Synthesis of Metal Oxides for Energy and Environmental Application

A thesis submitted towards partial fulfilment of
BS-MS Dual Degree Programme

by

Tanya Kumari

under the guidance of

Dr. Satishchandra B. Ogale
National Chemical Laboratory-Pune

Indian Institute of Science Education and Research
Pune

Certificate

This is to certify that this thesis entitled "SYNTHESIS OF METAL OXIDES FOE ENERGY AND ENVIRONMENTAL APPLICATION" submitted towards the partial fulfilment of the BS-MS dual degree programme at the Indian Institute of Science Education and Research Pune represents original research carried out by "TANYA KUMARI" at "NATIONAL CHEMICAL LABORATORY, PUNE", under the supervision of "Dr. SATISHCHANDRA B. OGALE" during the academic year 2013-2014.

Student

Tanya Kumari

20091085

Supervisor

Satishchandra B. Ogale

Chief Scientist, NCL Pune

Acknowledgement

With my deep sense of gratitude, I would like to thank my supervisor Dr. Shouvik Datta for giving me an opportunity to pursue my BS-MS final year thesis studies under his supervision. He has provided me to continuous support and guidance during my scientific research.

Further, it is my privilege to groom my scientific temperament under the mentorship of Prof. Satishchandra Ogale at the National Chemical Laboratory (NCL) for the whole year. His expertise in physics and material science has helped me to find solutions of some interesting scientific research problems. His innovative thinking, dedication towards science, oratory skills and commitment have always encouraged me to work sincerely. His moral and ethical behavior will guide me throughout my life.

I express my sincere gratitude to my senior PhD guide Onkar Game for his wonderful support throughout the year. My project has been completed under his sincere guidance. He has always shown confidence in my abilities to work independently which is very motivating. I thank him for his endless support filled with patience and enthusiasm during my whole project duration. I thank him for his critical comments and tremendous efforts in preparing this dissertation.

I would like to acknowledge DST for the Inspire scholarship provided for my BS-MS dual degree course. I am sincerely obliged to the Director, Indian Institute of Science Education and Research (IISER), Pune for giving me opportunity to study in the Institute.

I would like to thank my present senior lab-mates Dr. Sarika mam, Dr. Parwez sir, Abhik sir, Anil sir, Mandakini di, Dhanya di, , Aparna di, Mukta di, Shruti di, Meenal di, Pradeep sir, Yogesh sir, Umesh sir, Wahid sir, Ketaki di, Neelima di, Lily di, Satish sir, Vishal sir, Datta sir, Reshma di, Rohan di, , Shradha di, Rounak sir, Deepti di, Pooja di, Anirudha sir, Satyawan sir, and all lab interns at NCL for providing a stimulating atmosphere.

Besides, I would sincerely like to thank all my IISER friends for making this five years of education a wonderful experience. I would also like to acknowledge all my teachers throughout my life for their knowledge, inspiration and blessing.

I take this opportunity to thank my beloved family members for the sacrifices and dedication they have made. As it is not possible for me to acknowledge everyone individually so I genuinely and humbly offer my gratitude to all of them who have directly-indirectly co-operated and supported me during such an important journey of my life.

Abstract

The tremendous increase in population and rapid development has created serious threats like energy crisis and environmental degradation. The rising price of oil (petrol, diesel etc.) is threatening world's economies and also on the other hand, the pollution caused by burning of these fossil fuels are causing climate change which is a major source of environmental concern. There is an immediate need for the development of environmental friendly energy conversion and energy storage devices. With enhanced understanding and ability to control and manipulate nano-synthesis on a large scale, emphasis is now being laid upon novel applications of such materials. The most investigated of nanosystems are semiconductor noble metals, quantum dots and functional metal oxides. During the past few decades the work on metal oxides has witnessed considerable upsurge in the fields such as solar energy conversion, energy storage, water splitting, catalysis, photocatalysis etc.

In this work we have attempted to bring focus of efficient metal oxides to explore newer application domains in the field of energy and environment. These metal oxides can solve the problem of energy crisis as they can be efficiently exploited in fabrication better performing eco-friendly energy conversion and energy storage devices. This forms the brief introduction to the thesis and is presented in Chapter 1. A brief overview of the experimental techniques used for the synthesis of transition metal oxides is presented in Chapter 2 along with a general outline of the instruments and methods used for the characterization of these nanomaterials.

Chapter 3 is dedicated to Mesoporous Single Crystal (msc) TiO_2 for lithium ion battery (LIB). It comprises of the introduction of msc TiO_2 and battery, theory of LIB, synthesis of msc TiO_2, preparation of electrodes for LIB application, Characterization result and discussion on synthesized msc TiO_2, electrochemical measurements to analyze the lithium storage Capability of msc TiO2 in LIB including half cell studies of Li/MSC TiO_2 as well as full cell studies of $LiMn_2O_4$/MSC TiO_2.

Chapter 4 is about optimizing solar efficiency of three important kinds of solar cell i.e. dye sensitized solar cells (DSSCs), quantum dot sensitized solar cells (QDSSCs) and solid state solar cells using Zinc Stannate, Zn_2SnO_4 (ZTO) as an anodic material. Basically, it contains synthesis of Zinc Stannate nanostructures, fabrication of Zn_2SnO_4 based all three solar cell devices, Zinc Stannate characterization result and discussion as well as J-V characteristic curves of Zn2SnO4 based all three solar cells for Performance evaluation.

Contents

Chapter 1

Introduction

1.1 Introduction and Motivation

In this fast growing world energy crisis is becoming one of the most important problems at a global scale. Today approximately 36 % of energy is obtained from oil, 24 % from gas, 28 % from coal, 6 % from nuclear source, 6 % from hydro-power source and 1 % from renewable sources like wind and solar energy. We have started facing the problem of depletion of available non renewable sources of energy which are seen in the form of frequent power cut, day by day increase in the price of diesel, petrol etc. The rising price of oil (petrol, diesel etc.) is threatening world's economies and also on the other hand, the pollution caused by burning of these fossil fuels are causing climate change which is a major source of environmental concern. Non renewable sources of energy like coal and petroleum require costly explorations with potentially dangerous mining and drilling, and they will become more expensive as these sources are getting exhausted rapidly.

There needs to be immediate shift in our energy sources from non renewable to renewable energy sources like sun, wind, hydropower, biofuels (that are grown and harvested without fossil fuels) etc. Renewable energy source is reliable and plentiful and will potentially be very cheap if technology and infrastructure regarding its extraction and supply improve. Renewable energy produces very minute amount of carbon related gases and therefore helps in restoring climate change caused by fossil fuel usage. If we consider renewable energy sources then solar energy is the first thing that comes into our mind. Because, every hour the sun radiates more energy (3 X 1024 J) onto the Earth's surface than is consumed globally (3.5 X 1020 J) in one year. To harness the power of solar energy efficiently, improvements in the efficiency of photovoltaics (solar cell) and electrical storage (battery) is essential. Because today's photovoltaic systems are used to generate electricity to pump water, light up the night, charge batteries, activate switches, supply power to the utility grid etc. and battery is used to

store the direct current (DC) electrical energy produced by these photovoltaics in chemical form so that it can be transported easily from one place to another as well as to deliver a relatively constant supply of power to electrical loads regardless of the time of day or weather conditions. Therefore improvement in efficiency of photovoltaic cell and battery is extremely important for our better future.

1.2 History of photovoltaic cell

The photovoltaic effect was first observed in 1839 by Alexandre Edmond Becquerel via an electrode in a conductive solution exposed to light. The first conventional photovoltaic cells were produced in the late 1954 at Bell Laboratories and were principally used to provide electrical power for earth-orbiting satellites. In the 1980s, photovoltaic cells became a popular power source for consumer electronic devices like watches, calculators, radios, lanterns and other small battery-charging applications. After the energy crisis of the 1970s, significant efforts were made to develop photovoltaic power systems for commercial and residential uses. To minimize the cost of solar cells for commercial purpose dye sensitized solar cells were given much importance in later years. The modern version of a dye sensitized solar cell, also known as the Grätzel cell was invented by Michael Grätzel in 1991 and he has been awarded the 2010 Millennium Technology Prize for this invention. Currently solid state solar cell is gaining much attention due to its high efficiency achievement.

1.3 History of battery

In 1800, Alessandro Volta described the first electrochemical battery called the voltaic pile. Voltaic pile consists of zinc and copper plates which were separated by a brine soaked paper disks which could produce a steady current for a considerably longer time. In 1836, British chemist John Frederic Daniell invented the Daniell cell which was the first practical source of electricity. In 1868, French chemist Georges Leclanche designed a wet cell. In 1992, Energizer introduced world's first AA Lithium battery.

Nanotechnology which exploits nanomaterials (materials of dimension smaller than 100 nm) possesses tremendous potential to solve many scientific and technological challenges faced by mankind to solve the problem of energy generation and energy storage. Selection of correct nanomaterials is very crucial in this regard. Currently metal oxides are widely used nanomaterials for optoelectronic applications because of more charge carrier density than any other class of nanomaterials.

1.4 Metal Oxides

Metal oxides are those chemical compounds which contain one or more oxygen atoms as anion (oxidation state of -2) and one or more metals (same/different) as cation. The very first question that arises is that why we use metal oxides for synthesis of various optoelectronic devices and why not metal for this purpose? The reason is that metal oxides have the advantage over metal electrodes for low-work-function electrodes. Nanomaterials with lower work functions generally facilitate faster electron emission because work function is the interfacial parameter of the surface of a material that determines how easily electrons can escape into a vacuum or gas environment. The metals that have low work functions, such as calcium (Ca) and magnesium (Mg), tend to be very reactive, and when in contact with organic molecules they will break the molecule's chemical bonds. On the contrary, low-work-function oxides are chemically inert, such as zirconium oxide (ZrO_2) and titanium oxide (TiO_2). Among all metal oxides transition metal oxides are always preferred because these oxides can be used to tune electrode work functions in order to maximize V_{oc} (open circuit voltage). They have a wide range of work functions. For example, oxides of titanium, zinc, tantalum, and zirconium—such as TiO_2, ZnO, Ta_2O_5 and ZrO_2—have low work functions and can be used as cathode while other oxides of molybdenum, nickel, copper, and vanadium—MoO_3,NiO, CuO and V_2O_5—have high work functions and can be used as anode in optoelectronic devices. Applications of metal oxides are huge as shown below in fig. 1.1.

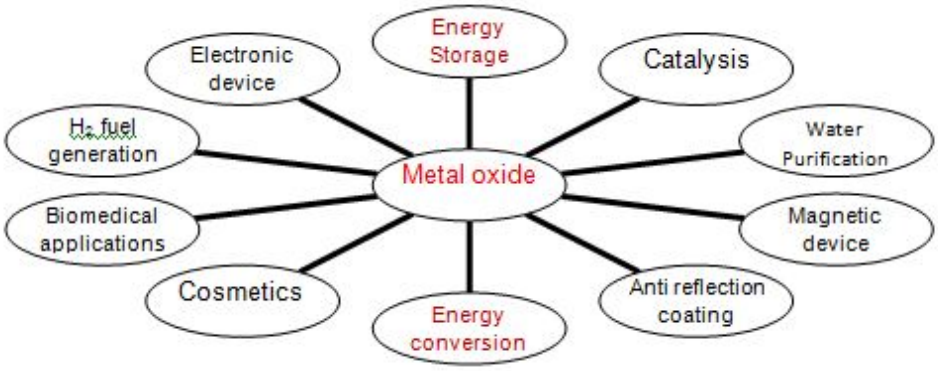

Figure 1.1: Schematic diagram of applications of Metal Oxides

Chapter 2

Experimental and Characterization Technique

2.1 Synthesis Techniques

Over the decades researchers have developed and adopted various synthesis techniques like hydrothermal method, thermal evaporation, pulsed laser deposition, spin coating, electrospinning, sol-gel method, chemical vapour deposition etc. Since the morphologies and properties of nanomaterials and composites mainly depend upon their synthesis methods and therefore, synthesis of nanomaterials is the most crucial and challenging step for the efficient use of these nanomaterials in several potential applications. Few synthesis techniques that we have used for synthesis as well as thin film deposition are discussed below.

2.1.1 Hydrothermal method

Hydrothermal reaction can be defined as any heterogeneous reaction in the presence of aqueous solvents under high pressure and temperature conditions to dissolve and recrystallize materials that are relatively insoluble under ordinary conditions. Supercritical water and supercritical fluids (SCF) provide an excellent reaction medium for hydrothermal processing of nanoparticles, since they allow varying the reaction rate and equilibrium by shifting the dielectric constant and solvent density with respect to pressure and temperature, thus giving higher reaction rates and smaller particles. The reaction products are to be stable in SCF leading to fine particle formation. This technique also facilitates issues like energy saving, the use of larger volume equipment, better nucleation control, avoidance of pollution, higher reaction rate, better shape control and lower temperature operations in the presence of the solvent. General structure of Teflon lined autoclave used for hydrothermal synthesis is shown in fig. 2.1.

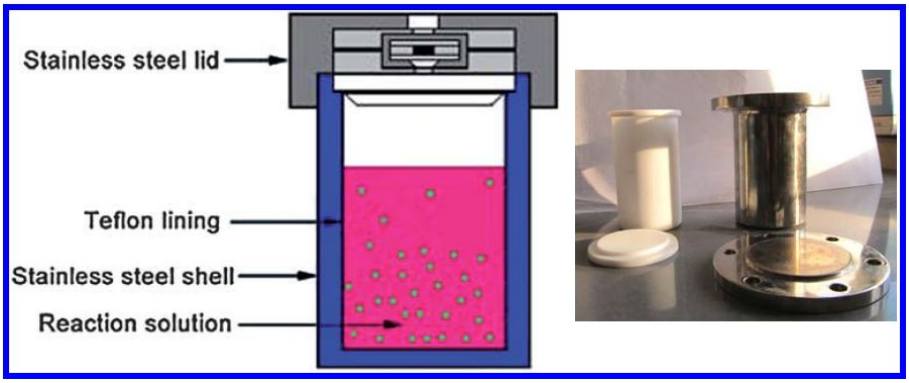

Figure 2.1: A typical Teflon-lined, stainless autoclave. The inset shows the photo of Stainless steel autoclave with Teflon liner typically used in the laboratory

2.1.2 Spin coating

Spin coating is a widely used technique for the thin film deposition of polymer resist layers which are commonly used in the lithographic patterning process[1]. Spin coating is a process which involves depositing a small amount of a solution onto the centre of a substrate as shown in fig. 2.2. This is then spun around at a high speed so that the solution is spread out by means of centrifugal force. The centrifugal force causes the excess solution to fly off the substrate and simultaneously, some of the solvent evaporates. The evaporation process raises the concentration and viscosity of the remaining solution. This high viscosity prevents the solution from exiting the substrate and a thin film of solution remains. Continued spinning evaporates the rest of the solvent after which a thin film of polymer is obtained. Factors such as rotational speed (rotation per minute i.e. rpm), acceleration, and fume exhaust contribute to how the properties of coated films are defined.

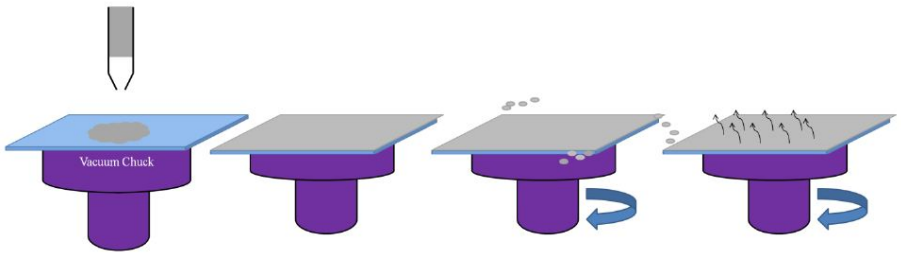

Figure 2.2: Schematic picture of spin coating technique

2.2 Characterization Techniques

A detail analysis of properties of the nanoparticles is very much important in order to employ them for any application. When dimensions of a synthesized material are reduced to nanoscale then their properties are quite different from their bulk nature. Structural, electronic and optical properties of a material drastically change when the size is reduced. Sometimes such changes in the properties can make the analysis a little complicated. Therefore it is very essential to choose the appropriate characterization technique which will give precise and clear information about the nanomaterials under study.

2.2.1 X-ray diffraction (XRD)

X-ray diffraction is a fast, non destructive analytical technique mainly used for the phase identification of a crystalline material. It also provides information on unit cell dimensions. XRD patterns are generated from the constructive interference pattern of elastically dispersed X-ray beams by atom cores. A constructive interference occurs only for certain θ's correlating to those planes (hkl), where path difference is an integral multiple (n) of wavelength as given by the Bragg's condition:

$$2d\sin\theta = n\lambda$$

Where d is the interplaner distance, 'θ' is the scattering angle, λ is the wavelength of the incident X-ray, and n is an integer (called order of diffraction). In nanostructures, X-rays peaks are obtained due to diffraction by the oriented crystallites at a particular angle which satisfy the Bragg's condition while other gets cancelled in the form noise. The resulting spectrum is a plot between the intensity recorded by the detector versus diffraction angle (2θ). Schematic view of XRD is shown in fig. 2.3:

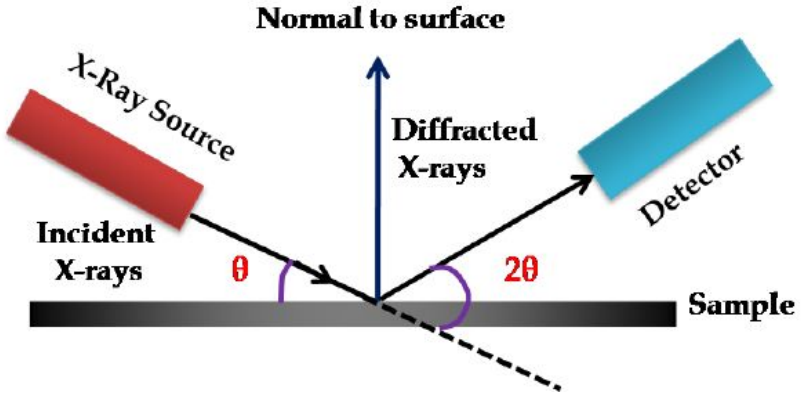

Figure 2.3: Representation of X-ray diffraction

2.2.2 Scanning Electron Microscope (SEM)

Scanning Electron Microscope uses a beam of electrons focused to a spot of approximately 1nm in diameter on the surface of the specimen and then scanned back and forth across the surface. The surface morphology of a specimen is revealed either by the backscattered (reflected) electrons or by electrons ejected from the specimen when the incident electrons ejects secondary electrons. A visual image corresponding to the signal produced by the interaction between the beam spot and the specimen at each point and along each scan line is simultaneously built up on the face of a cathode ray tube similar to the way that a television picture is generated. Schematic diagram of a scanning electron microscope with its components is shown in fig. 2.4:

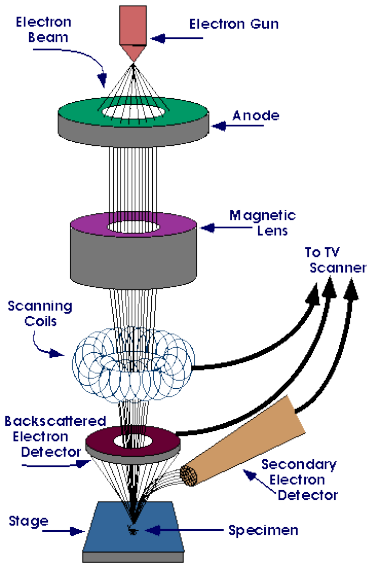

Figure 2.4: Schematic diagram of a scanning electron microscope (taken from http://www.purdue.edu/rem/rs/sem.htm)

2.2.3 Transmission electron microscope (TEM)

Transmission electron microscope is one of the most powerful techniques for the characterization of nanostructured materials as it allows one to achieve atomic resolution of crystal lattices. Due to the attached energy-dispersive X-ray spectroscopy (EDS) techniques, it can also be used to obtain chemical and electronic information at the sub-nanometer scale. The beam is passed through a series of lenses to obtain the magnified image. The Objective lens mainly determines the final image resolution. Further, when coupled with SAED (Selected Area

Electron Diffraction), the technique can provide important information on the crystallographic directions in the structures, helpful to understand the growth kinetics[2][3].

2.2.4 Diffuse reflectance spectroscopy (DRS)

Diffuse reflectance spectroscopy measurement with a UV-visible spectrophotometer is a standard technique for determining the absorption properties of materials[4]. In DRS mode the samples that are opaque is analyzed by placing them at the back of an integrating sphere, reflecting light off them, and gathering the scattered light that bounces back. DRS is used to calculate the energy gap of optically active semiconducting materials which can be determined by extrapolation of tangent to Tauc's plots[5] which is given as:

$[F(R)h\nu]^{1/n} = \alpha(h\nu - E_g)$

{F(R) is modified Kubelka-Munk function: F(R) = (1-R)^2/2R}

Where, R is reflectance measured from DRS of samples, h is Planck's constant, ν is the frequency of light, α is the proportionality constant, E_g is the band gap energy and n is a number (n =1/2 for direct band gap material while n = 2 for indirect band gap material).

2.2.5 Solar Cell Efficiency Measurement

Few important terms related to the performance of a solar cell like fill factor and conversion efficiency are defined by parameters such as short-circuit current Isc and open-circuit voltage Voc obtained under standard illumination conditions (AM 1.5).

Open Circuit voltage (Voc) and short-circuit current Isc:

The open circuit voltage (Voc) is the maximum voltage, when the circuit resistance has caused current to cease flowing. The Voc is measured under the condition when there is no external load connected, i.e. when the impedance is low and the current passing through the cell is 0. The short circuit current (Isc) is the maximum current through the circuit when there is no resistance (and hence no voltage) and thus it is calculated when the voltage equals 0.

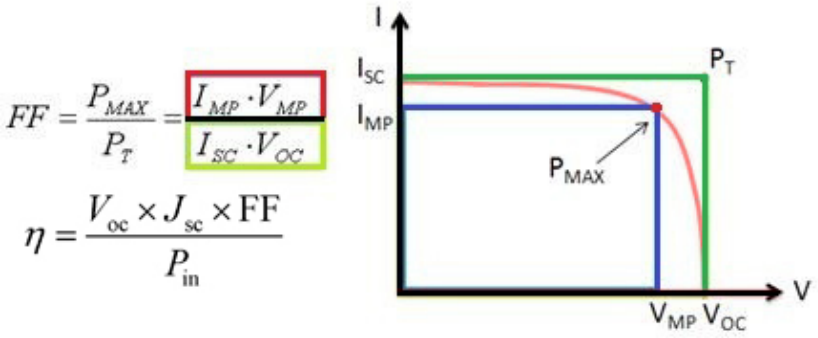

Figure 2.5: General I-V curve for a solar cell along with fill factor and conversion efficiency.

Fill factor (FF):

It is defined as the ratio of the actual maximum obtainable power to the product of the short circuit current and open circuit voltage. DSSC with a high fill factor have a high equivalent shunt resistance and a low equivalent series resistance, therefore, less amount of the current produced by the cell is dissipated due to internal losses.

Conversion efficiency (η):

It is defined as the ratio between maximum power generated by a cell and the incident power Pin. The incident power for efficiency calculations is 1 kW/m2 or 100 mW/cm2 (with an air mass, AM 1.5 spectrum).

Generally instead of I-V curve, we plot J-V curve i.e. voltage (V) vs. current density (J) because J-V curve is a normalized curve whose results can be compared with others result as current density (current per cm^2 area) is a normalized value.

Incident photon-to-current conversion efficiency (IPCE) Measurements:

The performance of a solar cell is quantified by the external quantum efficiency or the incident photon to current conversion efficiency (IPCE). IPCE specifies how efficiently the device under test (DUT) ejects electrons for each photon of a given wavelength. IPCE values provide practical information about the monochromatic quantum efficiencies of a solar cell[6] (IQE). This value gives the percentage of photons absorbed by the DUT that are converted into electrons as a function of wavelength. If the absorption spectrum of the device under test is known, the fraction of absorbed photons can be used to calculate the internal quantum efficiency The IPCE value corresponds to the photocurrent density produced in the external circuit under monochromatic illumination

of the device divided by the photon flux that strikes the device. From such an experiment the IPCE as a function of wavelength can be calculated from

$$IPCE = \frac{J}{\phi_\lambda}$$

Where, e is the elementary charge, J is the current density and ϕ_λ is the incident photon flux.

2.2.6 Electrochemical measurements for the performance of Lithium ion battery

Cyclic Voltammetry (CV) Curve:

Cyclic voltammetry is a kind of potentiodynamic electrochemical measurement. In a CV experiment the potential of working electrode is ramped linearly versus current (similar to linear sweep voltammetry), however when cyclic voltammetry reaches a set potential, the potential ramp of working electrode is inverted. Thus, the potential scans are taken for a particular potential window in a cyclic manner. The cyclic voltammogram trace is obtained by plotting the current at the working electrode versus the applied voltage to give. Fig. 2.6(a) represents a cyclic voltammetry curve in which appearance of a pair of sharp cathodic and anodic peaks can be seen which corresponds to the faradic insertion and extraction of lithium into anode (say TiO_2). Those sharp peaks appear at two different voltages although ideally they should appear at same voltage. This could be due to inefficient extraction of Li+ ion from anode material while discharging. CV curve provides lots of information about the electrode and electrode/electrolyte interaction.

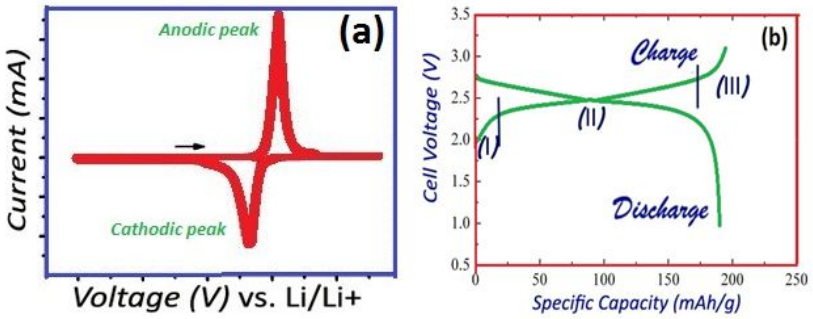

Figure 2.6: (a) Cyclic Voltammetry curve and(b) Galvanostatic charge discharge curve

Galvanostatic charge-discharge curve:

Galvanostatic charge-discharge measurement is a chronopotentiometric technique which is used to characterize the electrochemical properties of insertion materials. Chronopotentiometry is a technique in which a current pulse is applied to the working electrode and its resulting potential is measured against a reference electrode as a function of time. In the galvanostatic charge discharge measurement for a battery; current reversal is used to estimate the specific capacity and cyclic chronopotentiometries are used to evaluate the cycling stability of the battery. Fig. 2.6(b) represents a general galvanostatic charge discharge curve. If we look at the charging profile we can see that it is divided into three regions.

- The first region (I) is characterized by a potential gain attributed to the insertion of Li^+ ion and formation of the conductive Li_xTiO_2. The extent of this region is directly proportional to the specific surface area ofthe TiO_2.
- The second region (II) shows a plateau at a particular voltage which is because of the well-known two-phase mechanism as described above.
- The third region (III) shows a sloped curve. This is due to the process involving surface lithium storage. The extent of this region depends on the morphology (surface area) of the TiO_2.

Chapter 3

Mesoporous Single Crystal TiO_2 for Lithium ion battery application

3.1 Introduction

3.1.1 Mesoporous single crystal TiO_2

Titania (TiO_2) plays an important role as a photocatalyst and photoelectrode base material. The band gap of bulk TiO_2 lays in the UV region i.e. 3.2 eV for the anatase phase. TiO_2 exists in to three stable allotropic forms namely anatase, rutile and brookite. Among all three forms, anatase TiO_2 has been known for its high photocatalytic activity for decades[7]. The reason for high photocatalytic activity of anatase over other polymorphs is due to high conductivity of anatase phase which is also the reason because of which TiO_2 is considered as a potential candidate for Lithium ion battery (LIB) application. Mesoporous nanostructured materials have recently attracted strong interest, as their mesoporosity offers unique features such as open porosity in often hierarchical pore structures allows fast access of electrolyte species, reactive gases and even liquids. Mesoporousity provides the desired highly accessible surfaces but many applications also demand long-range electronic connectivity and structural coherence. A mesoporous single-crystal (MSC) semiconductor can meet both criteria. Therefore, utilizing properties of mesoporous single crystal TiO_2 for Lithium ion battery application would be advantageous. Conventional TiO_2 nanocrystals require in-film thermal sintering to make electronic contact between particles which also increases fabrication cost. We can use nanosized TiO_2 material which give a very high reversible capacity however a decrease of volumetric energy density due to connectivity loss between particles by parasitic reaction with electrolyte has already been reported. Therefore, correct morphology seems to be important in determining the electrochemical performance of

TiO_2 materials in Li-ion batteries. In this regard, mesoporous single crystals can acquire attention as mesoporousity provides highly accessible surface area for Li ion insertion and single crystals allows long range structural coherence as well as electronic connectivity. It is also very well known that mesoporous materials are effective in increasing electrode stability particularly at high charge/discharge rates. Till now lots of report on mesoporous anatase TiO_2 for application in LIB has been reported but, no report on MSC (mesoporous single crystal) anatase TiO_2 has been reported. For example, mesoporous anatase TiO_2 via a sol–gel method from a titanium precursor in the presence of a surfactant at pH 2 has been synthesized[8] and the excellent rate capability that has been reported[9] is of 184 $mAhg^{-1}$ at C/5, 158 $mAhg^{-1}$ at 2 C, 127 $mAhg^{-1}$ at 6 C, and 95 $mAhg^{-1}$at 30 C. Therefore in this report we synthesized single crystal mesoporous TiO_2 sample using a reported method and applied it for the Lithium ion battery.

3.1.2 Battery

Battery is one of the most common energy storage devices. It is also called as electrochemical cell. Batteries are those devices which store chemical energy and can convert this on demand to electrical energy in order to power several electronic applications. In battery electrical energy is generated by the conversion of chemical energy through redox reactions at anode and cathode. Since, reactions at anode usually take place at lower electrode potential than that of cathode therefore these are also termed as –ve and +ve electrode respectively. Specific energy (energy per unit mass) for batteries is much lower than common fuels such as gasoline. This is somewhat due to the fact that batteries deliver their energy as electricity (which can be efficiently converted to mechanical work), whereas using fuels have low efficiency of conversion to work. Batteries are generally of three types:

1. primary battery which can be discharged only once and then is discarded,
2. secondary battery or rechargeable battery that can be charged several times and can be reused and
3. batteries specially designed type used for military and medical purposes[10].

Among all the battery types, rechargeable batteries are the most popular and commonly used batteries because of its recharging nature. There are various types of rechargeable batteries such as nickel cadmium battery, lead acid battery and Li ion battery[11] Among all these, Li ion battery with high energy density and lighter weight has replaced most of the other batteries. Since we have studied Li ion battery aspects of single crystal mesoporous TiO_2, the focus of the ongoing discussion is on Li ion battery. We will start with brief introduction on Lithium ion battery.

Lithium ion battery (LIB):

Lithium ion battery (LIB) is a kind of rechargeable battery in which lithium ions (Li^+) move from the positive electrode (cathode) to the negative electrode (anode) while charging and vice versa while discharging. The performance of Li ion battery largely depends upon the anode and cathode materials. These batteries use an intercalated lithium compound as a cathode material instead of metallic lithium (as used in lithium battery). Anodic material should have very high accessible surface area for intercalation of large amount of lithium ions (Li^+) while charging.

3.2 Theory

While charging negative potential is applied to the negative electrode (anode) and positive potential is applied to the positive electrode (cathode). Due to this Li+ starts moving towards the anode side and gets intercalated into the anodic material which is characterized by the appearance of a sharp anodic peak in cyclic voltammetry curve. During this anodic material gets reduced. While discharging, the battery is connected to an external load and the process gets reversed. Anodic material is oxidized when lithium ions (Li^+) get deintercalated from this anodic material and intercalates back to the cathodic material as shown below in figure 3.1:

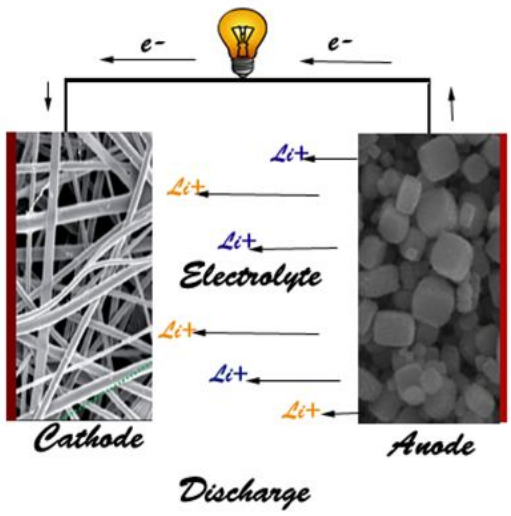

Figure 3.1: Discharge process in a typical lithium ion battery

The most common Li ion cell consists of carbon as anode and lithium cobalt oxide ($LiCoO_2$) as cathode. Lithium hexafluorophosphate ($LiPF_6$) salt with ethylene carbonate organic solvent mixture is used as electrolyte[12][13].

The basic reactions involved in charging and discharging cycles for $LiCoO_2$ and carbon based LIBs are as follows:

At cathode (during charging and vice-versa in discharging)

$LiCoO_2 \rightarrow Li_{1-x}CoO_2 + xLi^+ + xe^-$

At anode (during charging and vice-versa in discharging)

$6C + xLi^+ + xe^- \rightarrow Li_xC_6$

Net reaction (during charging and vice-versa in discharging)

$LiCoO_2 + 6C \rightarrow Li_{1-x}CoO_2 + Li_xC_6$

Since we have synthesized mesoporous single crystal anatase TiO_2 for lithium ion battery application, therefore very well known Li^+ insertion/extraction mechanism in TiO_2 has been explained below.

Lithium insertion-extraction mechanism in anatase TiO_2:

It is well known (both theoretically and experimentally) that during the Li^+ insertion, the tetragonal anatase TiO_2 phase is transformed into an orthorhombic phase ($Li_{0.5}TiO_2$) as:

$TiO_2 + xLi^+ + xe^- \rightarrow Li_xTiO_2, 0 \leq x \leq 1$

A spontaneous phase separation occurs between lithium-poor $Li_{0.01}TiO_2$ (tetragonal) and lithium-rich $Li_{0.5}TiO_2$ (orthorhombic) and this process is characterized by a constant voltage. It is well known that the two phases were in equilibrium with a continuous Li^+ ion flux operating between them. Besides this two-phase Li insertion process, an additional insertion process takes place at the surface of TiO_2 i.e. Li ions are also stored at the surface of anodic material besides intercalation. This surface storage mechanism is supposed to be responsible for the presence of pseudo-capacitance in the TiO_2 as well as in other material. It is now known that such mechanisms are strictly related to the porosity, the dimensions, and the surface area of the TiO_2.

3.3 Method

3.3.1 Synthesis of mesoporous single crystal TiO_2

Synthesis of mesoporous single crystal comprises of number of steps which has been mentioned below one by one.

Synthesis of mesoporous silica template:

50 nm silica spheres were synthesized as reported[14]. In typical synthesis, 49.5 ml of tetra ethyl orthosilicate, TEOS (sigma Aldrich) was added slowly in 375 of ethanol under constant stirring. Then 14ml D.I. water and 11 ml of ammonia sol. (25%, sigma Aldrich) was mixed and added dropwise to the above solution. It is constantly stirred for 24 hours at 700 rpm. It is then centrifuged at 7,000 rpm for 5 hours. Finally the product is annealed at 500°C for 30 min. (ramp time 150 min.).

Seeding of silica template:

Seeding of silica template is done according to the reported procedure[15]. 15 uM $TiCl_4$ aq. solution is prepared using HCl (1 drop) treated D.I. water (100 ml). 33 ml of the above solution is taken in a beaker and 5 g of the above sintered silica template is added into it. It is heated at 70°C for 60 minutes and then washed with 1 liter of D.I. water. Finally, the product is resintered at 500°C for 30 min. (ramp time 150 min.).

Meaoporous single crystal formation:

In 250 ml D.I. water 211.4 ul of HCl (35%) is added. 40mM Titanium tetra fluoride solution is prepared by adding 0.24772 g of TiF_4 in 50 ml of above solution. 1.67ml of ionic liquid (1-n butyl-3-methyl imidazolium tetrafluoroborate) is added into the above solution under constant stirring. 1 g of the $TiCl_4$ treated silica template is added to the above solution; stirred for some time and then finally hydrothermally treated at 190°C for 12 hours. Obtained product is washed with DI water several times and then etched for 1 hour in 170 ml of 2M NaOH solution at 80°C under constant stirring. Finally it is vacuum filtered and washed twice with D.I. water and twice with ethanol using PTFE filter paper of 0.2 um pore size.

3.3.2 Preparation of electrodes for lithium ion battery application

All electrochemical measurements to check the performance of lithium ion battery were carried out in a standard 2016 coin-cell configuration. Electrode

preparation for half cell and full cell assembly has been followed according to the reference[16].

For the half-cell configurations the composite electrodes were fabricated with 10 mg of accurately weighed msc TiO_2 or $LiMn_2O_4$ nanofibers (active material), 1.5 mg of teflonized acetylene black (TAB-2) and 1.5 mg of Super P. They were mixed to form the homogeneous mixture which was then pressed over a stainless steel mesh (0.25 mm thick) on an area of 200 mm2. It is served as a current collector. Half-cell assemblies of either Li/TiO_2 mesoporous single crystal or$Li/LiMn_2O_4$ nanofibers were assembled using metallic lithium (0.59 mm thick) as the reference and counter electrodes.

In the case of full cell assembly, anode-to-cathode mass ratio was balanced according to the electrochemical performance of anode and cathode in half-cell configurations. In both full-cell and half-cell assemblies, electrospun PVdF-HFP (poly(vinylidenefluoride-hexafluoropropylene)) membranes gelled with 1 M $LiPF_6$ in ethylene carbonate (EC)–di-methyl carbonate (DMC) mixture were added between electrodes. In this PVdF-HFP gel acts as a separator as well as an electrolyte.

3.4 Results and discussion

3.4.1 Characterization result and discussion

3.4.1.1 XRD

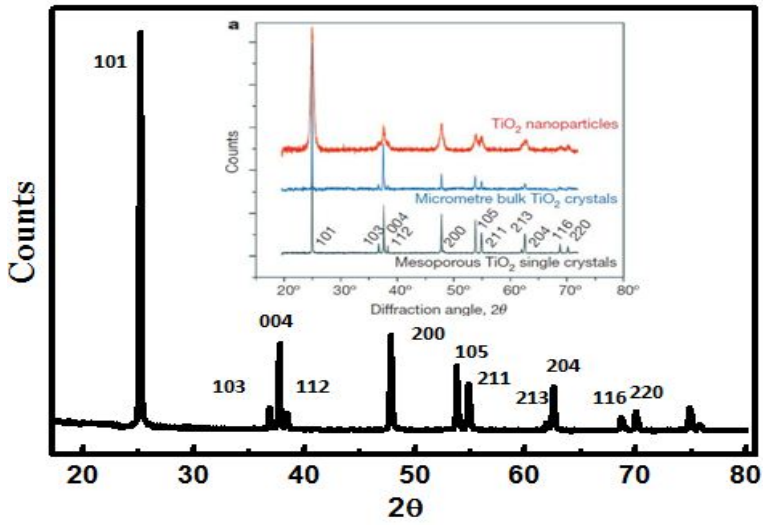

Figure 3.2: XRD of mesoporous single crystal TiO2 (inset: XRD image comparison purpose)

Fig. 3.2 shows the X-ray diffraction (XRD) pattern of the synthesized mesoporous single crystal anatase TiO_2. X-Ray diffraction (XRD) was recorded on a Philips X'Pert PRO using Cu Kα radiation. The anatase phase of synthesized TiO_2 samples was confirmed from the standard PCPDF database (# 861157). The inset image is taken from Henry Snaith's nature paper (doi: 10.1038/nature11936) for comparison purpose. The peak width of the TiO_2 crystals is very much narrower which indicates the presence of micron sized crystals. The approximate particle size of this sample was calculated using Debye Scherrer formula

$$\tau = \frac{0.94\lambda}{\beta Cos\theta}$$

Where, τ is the particle's domain size, λ is the wavelenth of radiation used, β is the full width at half maximum (FWHM) and $\theta$is the angle at maximum intensity.

Debye Scherrer formula gave the approximate particle size of as synthesized TiO_2 to be 52 nm.

3.4.1.2 SEM

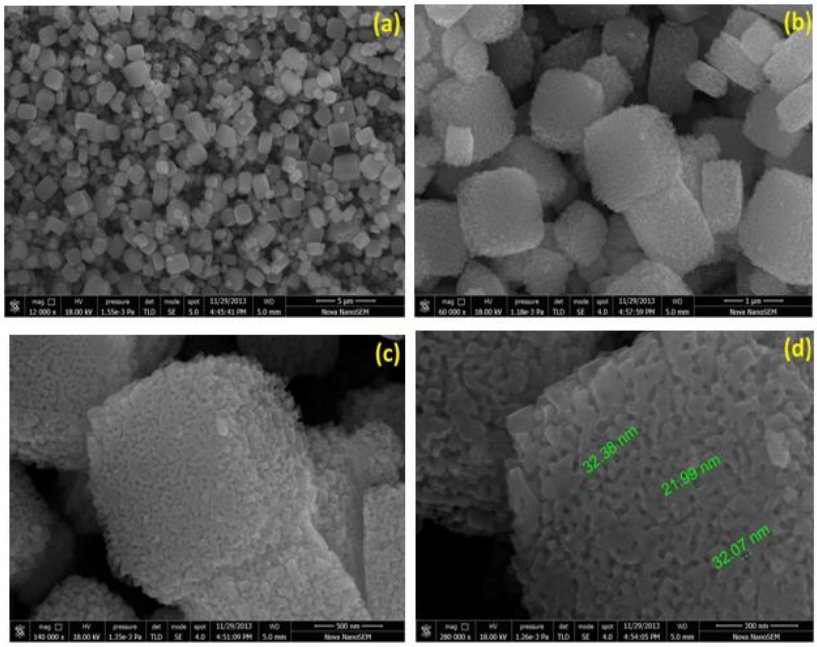

Figure 3.3: (a), (b), (c), (d) are the SEM images of synthesized mesoporous single crystal TiO_2 with image magnification of 5 um, 1 um, 500 nm and, 300 nm respectively

Fig. 3.3 (a), (b), (c) and (d) are the SEM (scanning electron microscopy) images of synthesized msc TiO_2 with different magnification. Fig. 3.3 (a) and (b) with magnification of 5 um and 1um respectively is taken to confirm that all the obtained particles are of same cubical morphology. Fig. 3.3 (c) with magnification of 500 nm shows the porous nature as well as approximate size of synthesized TiO_2 microcrystals to be 250 nm-2 um. Fig. 3.3 (d) with magnification of 300 nm is taken to measure diameter of each pore. It can be seen from this figure that the most of the pores are of the diameter ~ 20-30 nm which confirms the presence of mesopores in the nanocrystals. Also the pore size of mesoporous TiO2 sample matches well with that of size of SiO2 nanoparticles synthesized to prepare template.

3.4.1.3 TEM

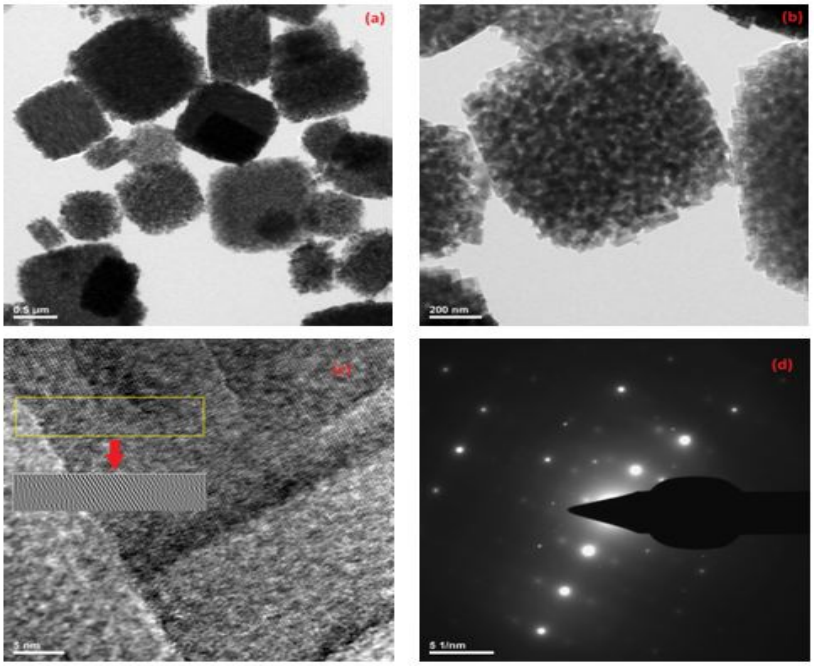

Figure 3.4: (a) and (b) are the TEM images of mesoporous single crystal TiO_2 with magnification of 0.5 um and 200 nm respectively, (c) the 5 nm magnified image of msc TiO_2 (inset: reduced FFT (Fast Fourier Transform) image of selected (yellow) region and (d) shows the SAED pattern of synthesized msc TiO_2.

In order to calculate the lattice parameter as well as to determine the single crystalline nature of mscTiO_2 , we have taken transmission electron microscopy (TEM) images and selected area diffraction (SAED) pattern respectively. Fig. 3.4 (a) and 3.4 (b) are the TEM images of msc TiO_2 with 0.5 um and 200 nm scale respectively. Fig. 3.4 (c) with inset image (reduced FFT) of selected region is taken to calculate the d_{hkl} spacing which is 3.7˚A for [101] peak. This d_{101} peak value is approximately in agreement with the theoretical value. Fig. (d) shows the SAED pattern of msc TiO_2 . One can see the dot pattern which implies that the synthesized mesoporous TiO_2 are single crystal in nature.

3.4.2 Electrochemical measurements to analyze the lithium storage capabilities of MSC TiO_2 in lithium ion battery

3.4.2.1 Half cell studies of Li/MSC TiO_2

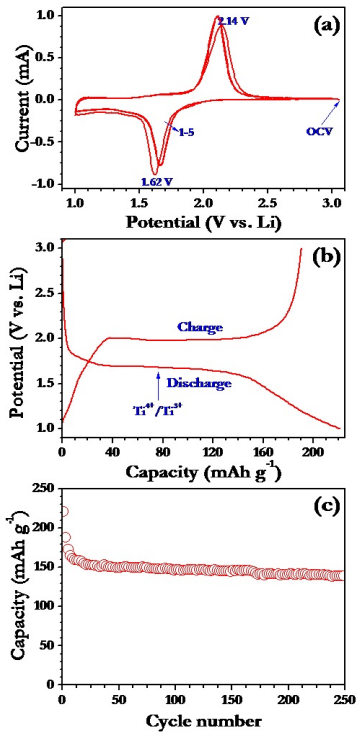

Figure 3.5: (a) cyclic voltammetry profile of mesoporous single crystal (msc) TiO_2 at a scan rate of 0.1 mVs^{-1} recorded between 1 and 3 V vs. Li in a half cell assembly, (b) galvanostatic discharge–charge curves of msc TiO_2 at current density of 150 mAg^{-1} and (c) plot of discharge capacity vs. cycle number for msc TiO_2 recorded in ambient condition

The cyclic voltammetry signature for msc TiO_2 is shown in Fig 3.5 (a). For CV signature of MSC TiO_2 , a slow CV scan at a scan rate of $0.1mVs^{-1}$ is performed and cycled between 1 and 3 V vs. Li. In this half cell assembly metallic lithium acts as both counter and reference electrode whereas TiO_2 electrode acts as working electrode. Cell showed an open circuit voltage (V_{OC}) of 3.0 V. In the first cycle presence of sharp cathodic (reduction) and anodic (oxidation) peaks is observed at 1.62V and 2.14V respectively. These reduction (Ti^{4+} to Ti^{3+}) and oxidation (Ti^{3+} to Ti^{4+}) peaks are mainly because of insertion and extrac-

tion of Li ion in TiO_2 framework respectively. The sharp oxidation/reduction peaks reveal the two-phase reaction mechanism during electrochemical lithium insertion/extraction according to the following equilibrium:

$TiO_2 + xLi + xe^- \leftrightarrow Li_xTiO_2$ (ref.[17])

However, in the subsequent cycles, small deviations in the peak positions are noted, possibly due to structural rearrangement of TiO2 crystal lattice as mentioned above. Overlapping of anodic peak during cycling corresponds to good life cycle of msc TiO2 however a small reduction and shift in the cathodic peak causes a minor capacity loss during successive cycles and is mainly because of other possible redox reactions happening during electrochemical process.

Fig. 3.5 (b) shows the galvanostatic charge-discharge curve for synthesized msc TiO_2 in a half cell assembly. From widely accepted mechanism of Li ion insertion/extraction we know that During intercalation tetragonal form of anatase TiO_2 changes to orthorhombic form according to the following equation:

$TiO_2 + xLi + xe^- \leftrightarrow Li_xTiO_2$ $0 \leq x \leq 1$

Due to this equilibrium exists between the lithium rich (orthorhombic- $Li_{0.5}TiO_2$) and lithium deficient (tetragonal- $Li_{0.01}TiO_2$) which is characterized by a constant voltage in the charge/discharge profile and has been well reported. Typical galvanostatic charge/discharge measurement is taken between 1 and 3 V vs. Li at a charging/discharging rate of 1C (1C $\approx$ current density of $150 mAg^{-1}$). Capacity of 220 and 190 $mAhg^{-1}$ is delivered for the first discharging and charging respectively.

Fig. 3.5 (c) shows the plot of discharge capacity vs. cycle number for synthesized msc TiO_2. The data points in the plot were collected after every 25 cycles. An irreversible capacity of 150 $mAhg^{-1}$ is achieved which is commonly reported for anatase TiO_2. Importantly the mesoporous TiO_2 sample when used as working electrode in half cell assembly gives a stable discharge capacity of 150 $mAhg^{-1}$ thereby proving the high stability of this material.

3.4.2.2 Full cell studies of $LiMn_2O_4$/ MSC TiO_2

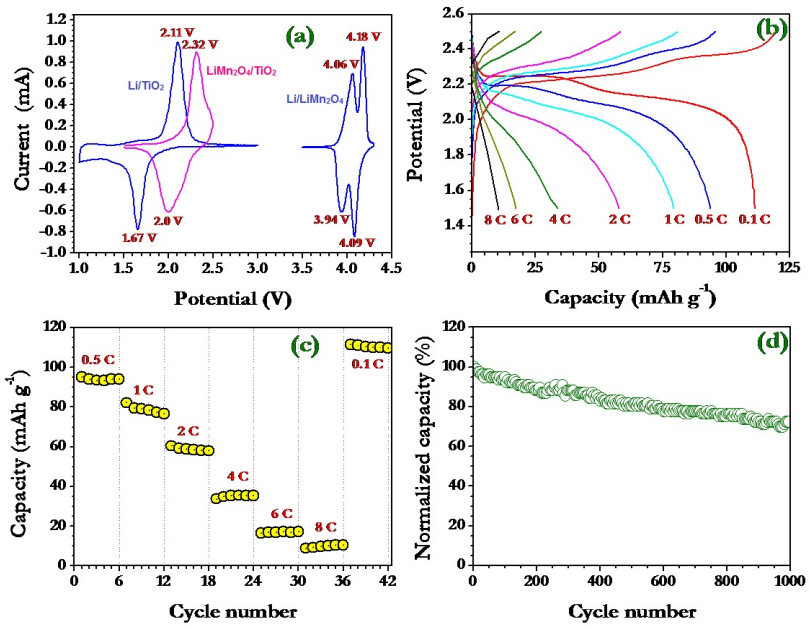

Figure 3.6: (a) Cyclic voltammetry curve (pink curve) of $LiMn_2O_4/TiO_2$ in full-cell assembly cycled between 1.6 and 2.5 V at a scan rate of 0.1 mVs^{-1} (blue curves are plotted to compare the performance of both $LiMn_2O_4$ cathode and TiO_2 anode in half-cell assembly for under the same scan rate), (b) typical galvanostatic charge–discharge curves for $LiMn_2O_4/TiO_2$ cells in full cell assembly cycled between 1.7 and 2.5 V at various current densities, C rates (1C is assumed as $150mAhg^{-1}$), (c) rate capability studies of $LiMn_2O_4/TiO_2$ cells cycled between 1.7 and 2.5 V at various C rates, and (d) long-term cyclability of $LiMn_2O_4/TiO_2$ cells cycled at 2 C rate.

The typical CV curves of $LiMn_2O_4/TiO_2$ in full-cell assembly cycled between 1.6 and 2.5 V at a scan rate of 0.1 mVs^{-1} has been shown in Fig. 3.6 (a). In this figure, the pink curve is for$LiMn_2O_4/TiO_2$ full cell which shows the presence of sharp peaks at ~2.32 and ~2.0 V during the anodic and cathodic scans, respectively. The anodic peak corresponds to the extraction of Li-ions from the cathode and simultaneous insertion of Li-ions into the anode (oxidation of Mn^{3+} to Mn^{4+} and reduction of Ti^{4+} to Ti^{3+}), whereas the cathodic peak is ascribed to the removal of Li from the TiO_2 and concurrent insertion into $LiMn_2O_4$ (oxidation of Ti^{3+} to Ti^{4+} and reduction of Mn^{4+} to Mn^{3+})[17]. The presence cathodic and anodic peaks having almost the same area under

the CV traces corresponds to the excellent reversibility during electrochemical cycling according to the following equilibrium:

$$LiMn_2O_4 + TiO_2 \leftrightarrow 2\lambda MnO_2 + LiTiO_2$$

Since polarization of the anodic MSC TiO_2 ($\triangle$V = 470 mV) in full-cell assembly is much higher as compared to cathodic$LiMn_2O_4/$ ($\triangle$V = 240 mV) in half-cell assembly due to which the two anodic and cathodic peaks observed in Li/$LiMn_2O_4$ half cell assembly is not evident in case of $LiMn_2O_4$//MSC TiO_2 full cell assembly[18].

In order to confirm the rate performance, the galvanostatic charge-discharge experiments were further performed at different current rates (C rates) from 0.1 to 8 C which is shown in fig. 3.6 (b). It be seen that a good reversible charge capacities are obtained at different C rates which show that MSCTiO_2 is a promising material for application in higher power lithium ion battery. However the decrease in capacitance with increase in C rates is due to the sluggish diffusion kinetics of Li ions at high rates[19].

Fig. 3.6 (c) shows the rate capabilities of $LiMn_2O_4$//MSC TiO_2 cell in full cell assembly at different C rates. Good rate capability and excellent cycle life with a capacity Retention is achieved irrespective of the various C rates (from 0.1 to 8C). It is known that with increase in the current rate decrease in capacity profile is observed this could be possibly because of the fact that the two phase equilibrium could be achieved for longer time at higher C rate.

Long-term cyclability measurement is performed at 2 C rate in fig. 3.6 (d) and it is shown in terms of normalized values (the initial discharge capacity 60 $mAhg^{-1}$ is assumed as 100%). The data points are collected after every 20 cycles. A very interesting cycling profiles are observed for 1000 cycles with capacity retention of ~70%, which is mainly due to the presence of mesoporousity in the anodic MSC TiO_2 which allows the spreading of electrolyte solution over large accessible area enabling facile Li^+ transport properties at high current rates[20].

3.5 Conclusion

In conclusion we synthesized micron sized (200 nm -2 um) anatase TiO_2 single crystals using hard template based hydrothermal method. The anatase phase of TiO_2 micro-crystals was confirmed using the x-ray diffraction and the approximate particle size was calculated from Debye Sherrer equation to be (52 nm) The as synthesized TiO_2 powder has cubical morphology which was confirmed from SEM. The single crystalline nature of TiO_2 was confirmed from the SAED pattern in TEM. The as synthesized TiO_2 sample was tested for the Lithium

ion battery performance in both half cell as well as full cell assembly. The mesoporous single crystal TiO_2 sample showed a stable and reversible cyclic capacity of 150 $mAhg^{-1}$. High performance and good cycling stability have been obtained for synthesized mesoporous single crystal TiO_2.

Chapter 4

Synthesis of Zinc Stannate (Zn_2SnO_4) for Solar cell application

4.1 Introduction

First half year of my project was dedicated to synthesis, characterization and application of Zinc Stannate (Zn_2SnO_4) nanoparticles for Dye sensitized solar cell (DSSCs), Quantum dot sensitized solar cells (QDSSCs) and solid state sensitized solar cells.

4.1.1 Zinc Stannate, Zn_2SnO_4 (ZTO)

Zinc Stannate, Zn_2SnO_4 (ZTO) is a ternary wide bandgap semiconductor with a bandgap of around 3.6 eV (Eg = 3.6 eV), but the precise bandgap energy depends on the synthesis conditions. It is a transparent conducting oxide with high electron mobility, high electrical conductivity, low visible absorption, and is used widely as gas sensors, electrode materials, and photoluminescence materials. It has also attracted considerable interest because of its high photocatalytic activity. It has face-centered cubic spinel structure[22]. Spinel structure with general molecular formula AB_2O_4 has the structure in which A^{+2} is in tetrahedral sites and two B^{+3} are in octahedral sites of cubic lattice. Inverse spinel structure for Zn_2SnO_4 is shown below in Fig. 4.1:

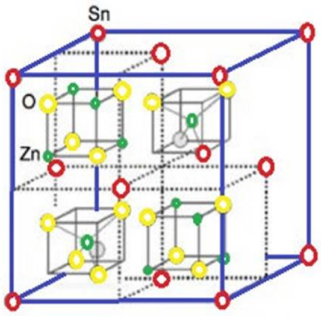

Figure 4.1: Face centered cubic spinel structure of Zn_2SnO_4

ZTO nanostructures can be produced using a variety of methods like thermal evaporation, high-temperature calcinations, mechanical grinding, sol-gel synthesis, hydrothermal reaction, and ion-exchange reaction etc. We have synthesized ZTO nanostructure using hydrothermal reaction method.

4.1.2 Solar Cell (photovoltaic cell)

Solar cell, also known as photovoltaic cell is an optoelectronic device which converts solar energy into electrical energy by means of photovoltaic effect. Photovoltaic effect is basically the generation of a potential difference at the junction of two different materials in response to irradiation with visible or other radiation. This process consists of mainly three steps:

- The generation of the electron-hole pairs or excitons due to the absorption of photons by the materials that form a junction.
- Separation of photo generated charge carriers at the junction.
- Collection of these charge carriers at the opposite terminals of the junction.

There are various types of solar cells like dye sensitized solar cell, quantum dot solar cell, hybrid solar cell, solid state solar cell etc.

Quantum dot sensitized solar cells (QDSSCs)

Quantum dot sensitized solar cells[23] (QDSSCs) are those solar cells which use quantum dots as a sensitizer instead of dye molecule. Quantum dots have tunable bandgaps across a wide range of energy levels by changing the size of quantum dots. This is very beneficial as compared to the bulk materials, where the bandgap is fixed according to the material composition. This tunable bandgap property makes quantum dots popular for solar cells. I have used Cadmium sulphide, CdS as a sensitizer in QDDSCs which is a direct band

gap semiconductor with a band gap of 2.42 eV. CdS has been deposited on Zinc Stannate films by very well known Successive Ionic layer Adsorption and Reaction (SILAR) method.

Solid state solar cells

Solid state solar cells are those solar cell which uses solid based electrolyte. Recently perovskites are used in place of liquid electrolyte. Now a days perovskites based solar cells are gaining much importance because of relatively higher efficiency and longer life as compared to dye sensitized solar cells. Perovskite is any material which has the perovskite structure i.e. calcium titanium oxide ($CaTiO_3$) structure. Perovskite material has general formula as ABX_3 ($^{XII}A^{2+VI}B^{4+}X_3^{2-}$) with oxygen atoms in the face centers of the lattice.

Dye sensitized Solar cells (DSSCs)

A DSSC is an efficient type of thin film photovoltaic cell which mainly consists of a transparent conductive oxide, TCO layer (Fluorine doped Tin oxide, FTO) on a glass, a wide-band-gap transition metal oxide (which is the electron acceptor), a layer of a chromophore sensitizer (molecular dye like N719) that absorbs light in visible region, a solid-state or a liquid-based redox medium (hole conductor medium typically an $I3^-/I^-$ redox couple in a liquid electrolyte), and a platinum-coated FTO glass (as the cathode). The wide-band-gap transition metal oxide along with the TCO and the dye (sensitizer) forms the photoanode of the cell. The liquid electrolyte is sandwiched between the photoanode and the platinum-based cathode. The structure of a dye sensitized solar cell along with its main components is shown in fig. 4.2:

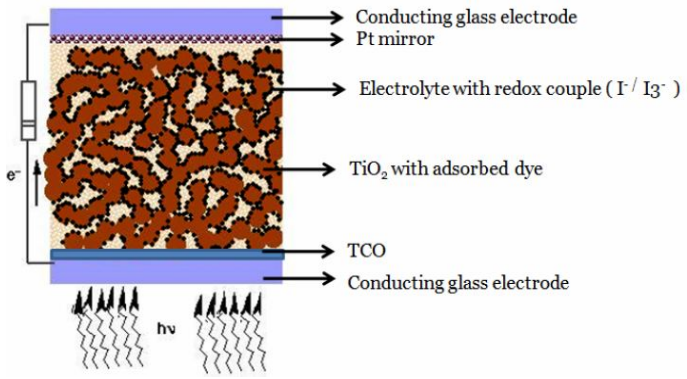

Figure 4.2: Illustrates the basic structure of the dye sensitized solar cell (DSSC).

4.2 Theory

As dye-sensitized solar cells (DSSCs) are promising candidate for renewable energy sources compared to silicon based or other solar cells due to its low production cost, light weight, flexibility, relatively high efficiency and low environmental impact during fabrication etc. its working principle has been explained below in detail. Working principle of other two QDSSCs and solid state solar cells are similar to DSSCs.

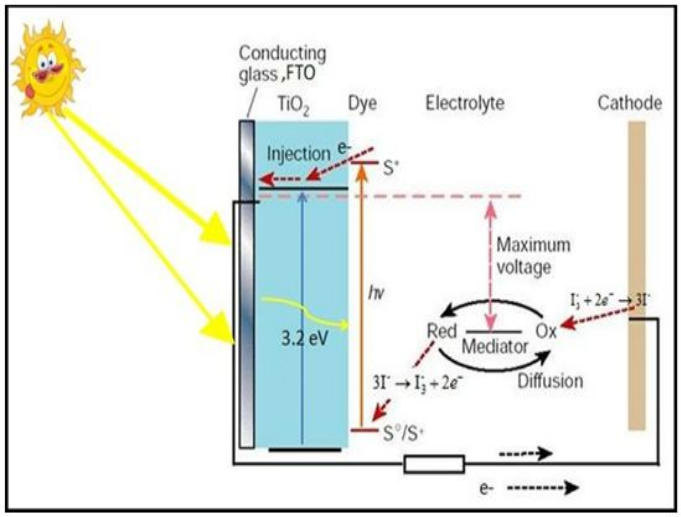

Figure 4.3: A TiO_2 based dye sensitized solar cell with all its component explaining its working mechanism.

As shown in fig. 4.3 when sunlight falls on cell from anodic side, it passes into the dye layer through the transparent electrode. The dye molecules absorb the photons and reach their excited state. The electrons in the excited state can either recombine with the holes of its valence band or can be injected into the conduction band of transition metal oxide (semiconductor). Since the electron injection process occurs faster (picoseconds) than the electron recombination process (microseconds) it allows charge separation to take place with high efficiency. Hence, dye molecule easily injects electrons directly into the conduction band of the semiconductor. The holes in the valence band of dye molecule accept electrons from the electrolyte to regenerate them as neutral molecules. The electrons injected into the semiconductor then move by diffusion to the anode FTO coated glass, from where they are moved to an external circuit. It should be noted that not all injected electrons reach the electron collector of the cell, because some react with I_3^- in the electrolyte at the electrode/electrolyte interface. This recombination process results in the decrease of the incident photon-to-current conversion efficiency. Electrons that successfully flow out through the

external circuit then return to the cathode (the platinum-coated FTO glass) of the cell. At the cathode, each triiodide ion, I_3^- in the electrolyte gets reduced by receiving two of the e^- returned to the cathode forming three I^- ions (as shown in fig. 4.3), which diffuse to the anode side of the electrolyte. At the anode, the oxidized dye molecules then strip electrons from I^- ions in the electrolyte, oxidizing the I^- ions back into I_3^- ions, which then diffuse to the cathode to complete the redox loop. The voltage generated under illumination corresponds to the difference between electrochemical potential of the electron at the two contacts, which generally for DSSC is the difference between the Fermi level of the mesoporous TiO_2 layer and the redox potential of the electrolyte. Transfer of electrons during cell operation involves following steps:

$TiO_2\|S + h\nu \rightarrow TiO_2\|S^*$ Excitation of dye upon irradiation (1)

$TiO_2\|S^* \rightarrow TiO_2\|S^+ + e^-$ Oxidation of dye due to e- injection into TiO_2 (2)

$TiO_2\|S^+ + e^- \rightarrow TiO_2\|S$ Dye recovers its original ground state (3)

$TiO_2\|S^+ + \frac{3}{2}I^- \rightarrow TiO_2\|S + \frac{1}{2}I_3^-$ Oxidization of the electrolyte (4)

$\frac{1}{2}I_3^- + e^- \rightarrow \frac{3}{2}I^-$ Electrolyte restoration at the counter electrode (5)

$I_3^- + 2e^- \rightarrow 3I^-$ Redox reaction (6)

In the field of dye sensitized solar cells the maximum efficiency achieved till now is 15 % by Gratzel for TiO_2 based dssc.

4.3 Method

4.3.1 Hydrothermal Synthesis of Zinc Stannate nanostructures

We have used hydrothermal method for synthesis of Zn_2SnO_4 because it has advantages over methods, such as a lower reaction temperature and simpler method for synthesizing nano-sized particles. Synthesis procedure[24] is shown with the help of diagram given below in fig. 4.4

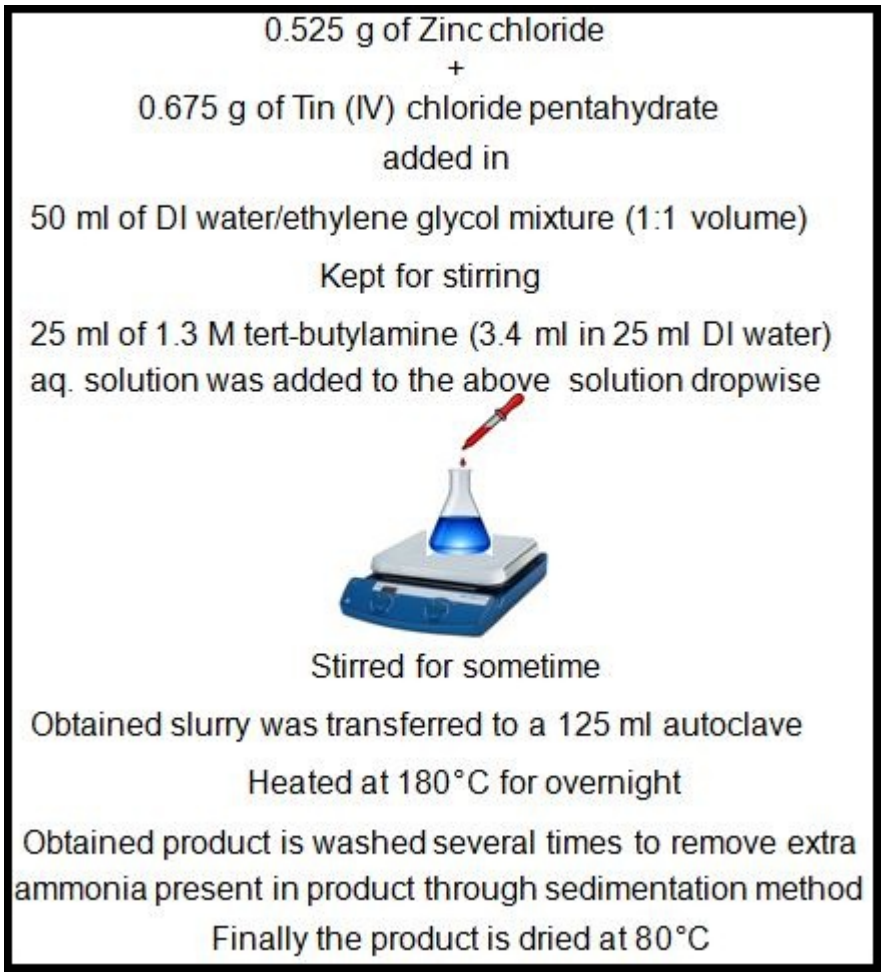

Figure 4.4: Systematic procedure for hydrothermal synthesis of Zinc Stannate nanoparticles

4.3.1.1 Preparation of Zn_2SnO_4 based paste and electrode for solar cell device

Preparation of Zn_2SnO_4, ZTO screen printing paste[25]

For Solar cell application ZTO paste were made using screen printing method as shown in fig. 4.5. At each step, liquids were added drop by drop into a porcelain mortar. It is made in the ambient air at room temperature. The Zn_2SnO_4, ZTO powders stuck on the inside of the mortar should be removed in order to grind large aggregates. To disperse Zn_2SnO_4 paste from the mortar, it is transferred with excess of ethanol to a beaker and stirred with magnet tip.

Take 1 g of Zinc Stannate (ZTO) powder and grind in a mortar (15min)
[Add 0.5 ml D.I. water to it and grind in the mortar for 5 min] X 5 times
[Add 0.5 ml ethanol in the above paste and grind it for 1 min] X 15 times
Transfer the ZTO paste to a beaker with using extra ethanol (3/4 vol. of beaker)
Stir with a magnetic needle (15 min), sonicate with probe sonicator [(2 sec on + 2 sec off) for 15 min], and again stir with the help of magnetic needle for 15 min
Add 3.5 ml of α- terpineol in the above solution
Stir with a magnetic needle (15 min), sonicate with probe sonicator [(2 sec on + 2 sec off) for 15 min], and again stir with the help of magnetic needle for 15 min
Add ethyl cellulose (0.45 g in 10 ml ethanol solution) and stir it for overnight
Probe sonicate it (15 min), then evaporate the ethanol with a rotary evaporator

Figure 4.5: Fabrication procedure of Zinc Stannate (ZTO) Screen printing paste.

Preparation of nanocrystalline Zn_2SnO_4(ZTO) electrode (anode)

For preparing the working electrode, the FTO glass was used as current collector (resistance $\approx$ 15 ohm/square). It was first cleaned in a detergent (liquid & powder) solution using an ultrasonic bath for 15 min, and then rinsed with water, ultrasonicated for 15 min and finally rinsed with ethanol and ultrasonicated for 15 min. These washed FTO coated glasses were air annealed at 450 °C for 10 minutes. A layer of paste was coated on the conducting side of FTO glass plates by doctor blade method and kept for drying in normal air. I did 5 layers coating of ZTO paste on FTOs for best result. It has been optimized by checking solar cell efficiency of ZTO films with different layer of coatings. Normally 5 layer coated ZTO thin films are $\approx$ 12-15 um thick. After each coating, films are subsequently heated and after final coating a sequential heating procedure is followed which is shown below.

- 1st layer coating of ZTO paste using doctor blade method then dried in air

- Heated at 200°C for 10 minutes
- Repeated this drying and heating procedure till final 5th layer coating of ZTO paste
- Finally sequential heating in programmable Nobertherm furnace is done as:

1. 200°C for 10 min
2. 325°C for 5 min
3. 375°C for 5 min
4. 450°C for 15 min
5. 500°C for 15 min

4.3.1.2 Device fabrication procedure of dye sensitized solar cells (DSSCs)

For dssc, the films are cooled to 70°C and then dipped into ruthenium based dye N719 for 12-24 hrs. For DSSCs ruthenium dye N719 as a sensitizer as shown in fig. 4.6 (a). Then the films are washed with ethanol. Then they are scratched from its side to get the area of 0.25 cm^2 at the center of the FTO glass. Then masking is done all around this area with the help of cellophane tape so that the cell does not get short circuit.

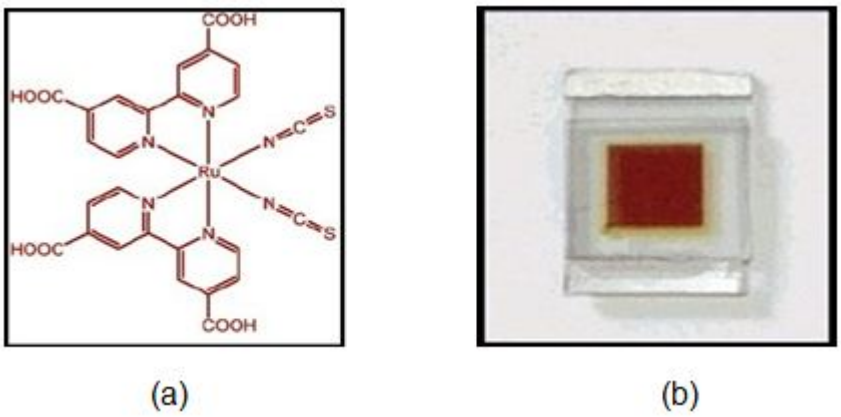

Figure 4.6: (a) Ruthenium dye N719 and (b) typical DSSC in full cell assembly

Platinum (Pt) coated counter electrode (cathode) is prepared by drop casting H_2PtCl_6 solution on a cleaned FTO coated glass. It is then air annealed at 450°C to make a uniform thin film of platinum. To prepare a full cell dye

sensitized ZTO film (anode) and Pt coated electrode (cathode) are sandwiched together with an iodine based electrolyte in between them. Typical image of a dssc in a full cell assembly is shown in fig. 4.6 (b).

4.3.1.3 Device fabrication procedure of quantum dot sensitized solar cells (QDSSCs)

For QDSSC, 5 layers coated ZTO films have been used for quantum dot sensitization. Here CdS quantum dots are used for sensitization (as it has a bandgap of 2.4 eV). In this case also platinum is used as a counter electrode but instead of iodine based, poly-sulphur based electrolyte is used because cadmium sulphides are not chemically compatible with this redox electrolyte. In aqueous electrolytes the electron flow corresponds to the photoanodic dissolution of CdS according to the reaction:

$$CdS \rightarrow Cd^{2+} + S + 2e^{-} \text{ (in light)}$$

Apparently CdS is regenerated by precipitation of the Cd^{2+} ions by the S^{2-} in the electrolyte. CdS quantum dots were deposited on ZTO films using SILAR (Successive Ionic layer Adsorption and Reaction) method which [26] is shown in fig. 4.7.

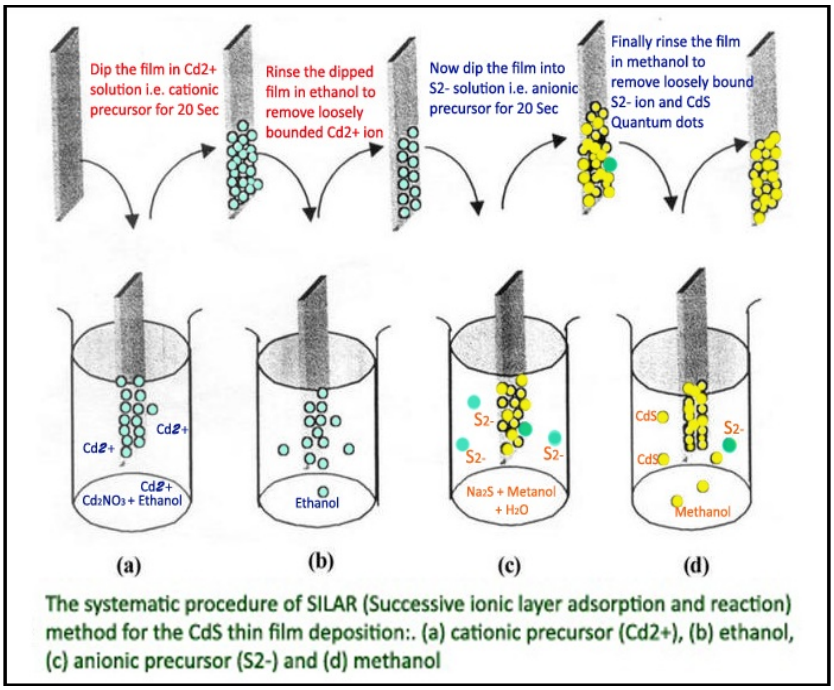

Figure 4.7: CdS quantum dot sensitization of ZTO thin films using SILAR method.

SILAR is a room temperature solution based process that can deposit atomic layers one layer at a time. The traditional SILAR cycle for a substrate is: (a) dipping into cationic precursor solution, (b) rinsing, (c) dipping into anion solution and (d) rinsing. I prepared 0.02 M $Cd(NO_3)_2.4H_2O$ in ethanol as cationic precursor solution and 0.02 M Na_2S in methanol + D.I. water (1:1 ratio) as anionic precursor solution. 10 cycles of CdS quantum dots were deposited on ZTO films with the procedure as shown in fig. 4.7.

4.3.1.4 Device fabrication procedure of solid State solar cell

For solid state solar cell; perovskite ($CH_3NH_3PbI_3$) was used for sensitization, spiro-MeOTAD[27] was used as a hole transporter (deposited by spin coating method) and gold coated electrode was used as a counter. The device fabrication method has been adopted from reference[28]. The device fabrication was carried out in a glove box (with humidity $<1\%$). The Zinc Stannate layer composed of 10-20 nm sized particles was deposited by spin coating (for 30 s at 5,000 rpm) using Zn_2SnO_4 paste (refer fig. 4.5: Fabrication procedure of Zinc Stannate (ZTO) Screen printing paste). The ZTO films were dried at 125 $^\circ C$ and then they were gradually heated to 500$^\circ C$ for 15 min and were finally cooled to room temperature. Before the use of the films, they were again heated at 500 $^\circ C$ for 30 min. For preparing $CH_3NH_3PbI_3$ perovskite (fig. 4.8 (a)) solution first of all PbI_2 was dissolved in N,N-dimethylformamide at a concentration of 462 $mgml^{-1}$ (~1 M) under constant stirring at 70 $^\circ C$. The ZTO films were then infiltrated with this PbI_2 solution by spin coating (for 90 s at 6,500 rpm) and then dried at 70 $^\circ C$ for 30 min. After cooling to room temperature, these films were dipped in a solution of CH_3NH_3I (in 2-propanol with concentration of 10 $mgml^{-1}$) for 20 s. Finally the films were rinsed with 2-propanol and dried at 70 $^\circ C$ for 30 min.

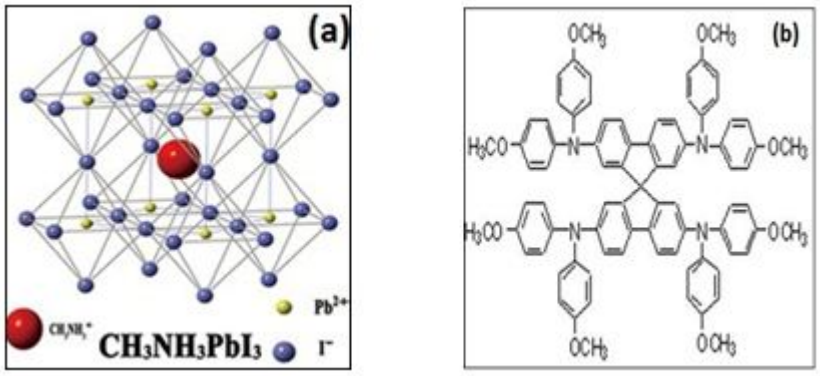

Figure 4.8: (a) Image of a CH3NH3PbI3 (perovskite) molecule and (b) a Spiro-MEOTAD (2,2',7,7'-tetrakis(N,N-di-p-methoxyphenylamine)9,9'-Spirobifluorene) molecule.

The spiro-MeOTAD (fig. 4.8 (b)) was then deposited by spin coating (for 30 s at 4,000 rpm). The spiro-MeOTAD solution for spin-coating was prepared by dissolving 72.3 mg (spiro-MeOTAD), 17.5 ul of a stock solution of $520 mgml^{-1}$ lithium bis(trifluoromethylsulphonyl)imide in acetonitrile, 28.8 ul 4-tert-butylpyridine (TBP) and 29 ul of a stock solution of 300 $mgml^{-1}$ tris(2-(1H-pyrazol-1-yl)-4-tert-butylpyridine)cobalt(iii) bis(trifluoromethylsulphonyl)imide in acetonitrile in 1 ml chlorobenzene. After this 80 nm of gold was deposited by thermal evaporation on top of the device to form the back contact.

4.4 Results and discussion

4.4.1 Zinc Stannate characterization result and discussion

The obtained products were characterized with X-ray diffraction (XRD), transmission electron Microscopy (TEM) and diffuse reflectance spectroscopy (DRS). X-Ray diffraction (XRD) was recorded on a Philips X'Pert PRO using $CuK\alpha$ radiation. XRD pattern as shown in fig. 4.9 (a) confirms that the product is pure Zn_2SnO_4 with the cubic inverse-spinel crystal structure. The approximate particle size was determined to be 15nm as obtained from the Debye-Sherrer equation.

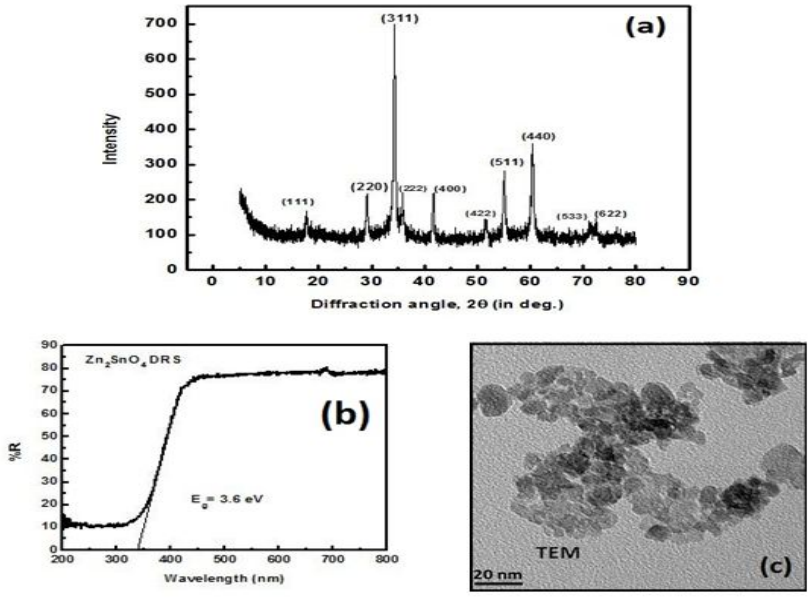

Figure 4.9: (a) XRD image of Zn_2SnO_4, (b) DRS curve of Zn_2SnO_4 and (c) TEM image of Zn_2SnO_4 nanoparticles.

UV visible diffused reflectance spectrum was recorded using a Jasco V-570 spectrophotometer which is shown in fig. 4.9 (b). From DRS a band-gap of 3.6 eV was determined for the synthesized Zn_2SnO_4 nanoparticles. A Low magnification TEM shows that the obtained nanoparticles are in the range of 10-20 nm as shown in fig. 4.9 (c).

4.4.2 Performance evaluation curves for Zn_2SnO_4 based solar cells

4.4.2.1 J-V characteristic curves of Zn_2SnO_4 based dye sensitized solar cells

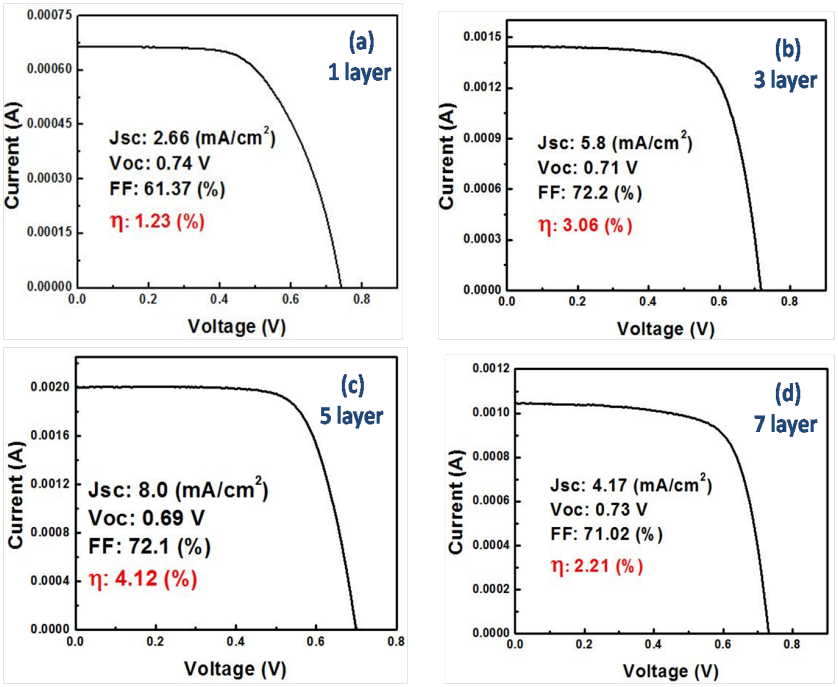

Figure 4.10: J-V characteristic of Zn_2SnO_4 dye sensitized solar cell (a) film with 1 layer of ZTO coating,(b) film with 3 layer of ZTO coating, (c) film with 5 layer of ZTO coating and (d) film with 7 layer of ZTO coating.

Fig. 4.10 shows J-V characteristics of Zn_2SnO_4 based dye sensitized solar cells. We have measured efficiency (η) of ZTO films up to 8 layers but, maximum efficiency has been achieved for 5 layers which is 4.12 % under 1 sun AM 1.5 illumination.1 layer ZTO coated dssc (fig. 4.10 (a)) shows the lowest efficiency (η) of 1.23%. The fill factor, FF (72.1%), current density, J_{sc} (2.66 mA/cm^2) and open circuit voltage, V_{oc} (0.51 V) are also lowest among all other dssc with

different layers of coating. This is because of the reason that 1 layer coated ZTO film has lesser dye loading as compared to other films hence, number of electrons ejected by these dye molecules upon irradiation is also less as compared to other films. Therefore due to the lack of sufficient charge carriers (electrons), solar efficiency and other parameters have lowest value. 3 layers ZTO coated film (fig. 4.10 (b)) shows intermediate value (between 1 and 5 layers coated ZTO films) for most of the photovoltaic parameters. 7 layers ZTO coated films (fig. 4.10 (c)) shows lower solar efficiency (2.21 %) as compared to 5 layers ZTO coated film. This can be due to the increased recombination for higher thickness of the film. The photoelectron injected in the higher thickness (7 layers) of ZTO has to travel larger path length which also increases the probability of recombination with electrolyte. Therefore, number of electrons actually reaching the collector gets significantly reduced which in turn gives lower efficiency.

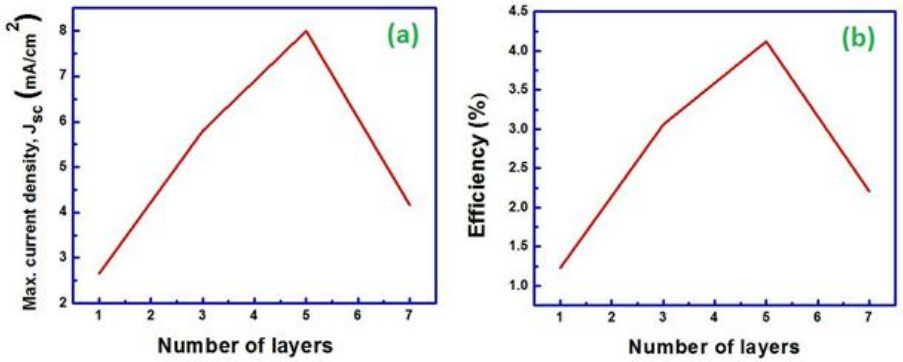

Figure 4.11: Comparison of solar cell parameters vs. no. of ZTO coated layer, (a) is a plot for comparing maximum obtained current density, J_{sc} vs. no. of layers and (b) is a plot for efficiency comparison.

Curves in fig. 4.11 show the dependence of photovoltaic parameters like current density and solar cell efficiency on the thickness of Zn2SnO4 (ZTO) coated through doctor blade method. Fig. 4.11 (a) and 4.11 (b) are plotted with the values obtained from the above J-V characteristic curves for different number of ZTO coated dye sensitized solar cells. It can be clearly seen that the best performance has been obtained for five layers coated cell. In conclusion we optimized the thickness of ZTO films in order to get maximum photovoltaic performance. The optimized ZTO films were then also tested for quantum dot sensitized solar cells described below.

4.4.2.2 J-V characteristic curve of Zn_2SnO_4 based quantum dot sensitized solar cells

A photocurrent density of 3.4 mA/cm^2, open circuit potential of 0.37V, a fill factor of 45.9% and overall power conversion efficiency of 0.61% was obtained

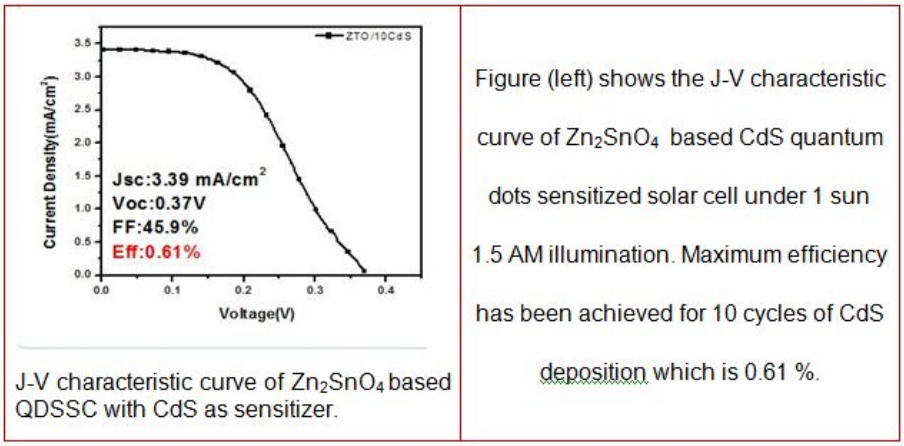

Figure 4.12: J-V characteristic curve of Zn_2SnO_4 based QDSSC with CdS as sensitizer.

for ZTO (5layers) and 10 SILAR cycles for CdS.

We have measured efficiency (η) of 5 layers coated ZTO films sensitized with CdS quantum dots up to 12 SILAR cycles but, maximum efficiency has been achieved for sensitization of 10 SILAR cycles.

4.4.2.3 J-V and IPCE curves of Zn2SnO4 based solid state sensitized solar cells

Liquid electrolyte based sensitized solar cells suffer from the drawbacks of sealing the device as improper sealing can lead to decrease in efficiency as well as it can cause the electrolyte to leak in the environment causing possible environmental hazards. Therefore there have been tremendous efforts so as to replace the liquid electrolyte with a solid state p type hole conductor. Also the photocurrents in liquid state DSSCs are limited by the absorption coefficient and light harvesting ability of the photo-sensitizer. Recently organo-metal halide perovskites were shown be much better light harvesting agents as compared to dyes because of their high absorption coefficient. Also a solid state p type hole conductor Spiro-MeOTAD was employed in the organometal halide sensitized solar cells making them promising alternative over the liquid electrolyte based DSSCs. The organometal halide perovskite sensitized solar employs similar design as DSSC in which the metal oxide plays the role of electron transport layer, perovskite plays the role of light absorber and the organic hole conductor plays the role of hole extraction layer. Herein we prepared the organometal halide perovskite based solid state solar cells with ZTO as electron transport layer. High electron mobility and transparency of ZTO makes it an attractive candidate for these solid state solar cells.

We measured the J-V characteristics curve of the Zn_2SnO_4 based solid state solar cells under simulated air mass 1.5 global (AM1.5G) solar irradiation (light intensity of 95.6 mWcm^{-2}). Curves shown below in Fig. 4.13 [(a), (b) and (c)] are J–V curves measured for cells in which Zn_2SnO_4 was spin coated at 2,000, 4,000 and 5,000 rpm so as to vary the thickness of metal oxide based electron transport layer. We can see the best performance is obtained for 4,000 rpm spin coated device (fig. 4.13 (b)) in which the short-circuit photocurrent (J_{sc}), the open-circuit voltage (V_{oc}) and the fill factor are 9.4 mAcm^{-2}, 0.95 V and 56.3 % respectively. The maximum efficiency achieved in this case is 5.02 %.

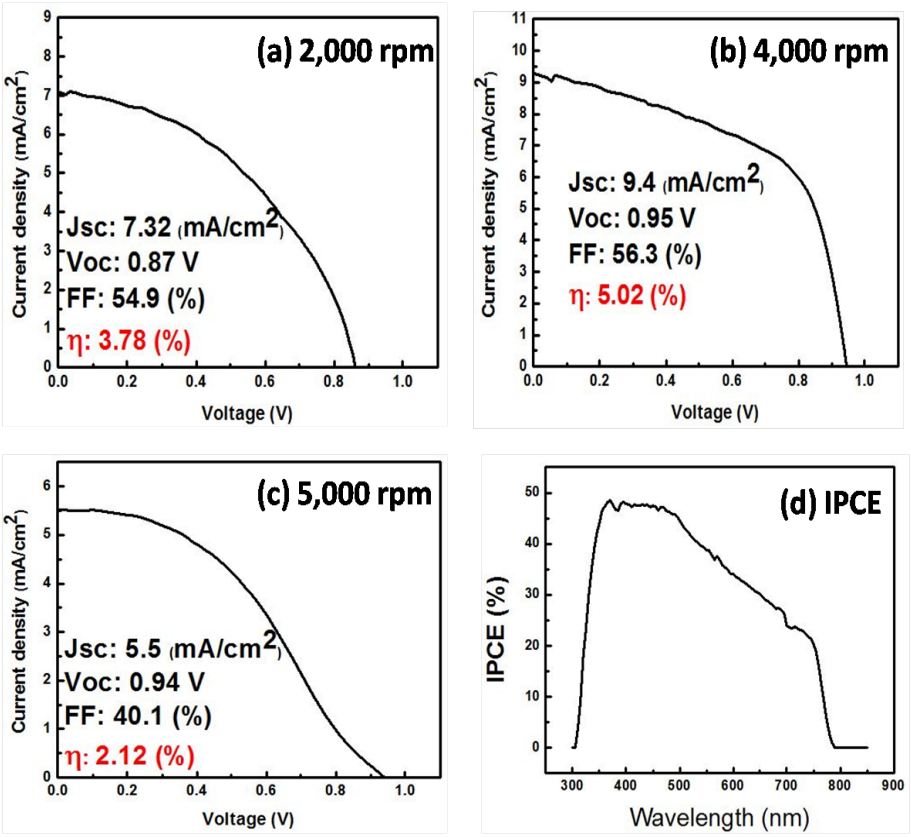

Figure 4.13: (a), (b), (c) the J-V characteristic curves of Zn_2SnO_4 based solid state solar cell where Zn_2SnO_4 was spin coated on FTOs at 2,000, 4,000 and 5,000 rpm respectively and (d) shows the IPCE spectrum for the best performing cell i.e. (b).

Fig. 4.13 (d) shows the external quantum efficiency or the incident-photon-to-current conversion efficiency (IPCE) spectrum for the best performing Zn_2SnO_4 based perovskite solar cell. Generation of photocurrent starts at approximately

790 nm which is in agreement with the bandgap of the $CH_3NH_3PbI_3$. It reaches peak value of 48% in the short-wavelength region ($\approx$ 370 nm) of the visible spectrum. Therefore the organometal lead halide can act as a better light harvesting agent as compared to dyes used in DSSC.

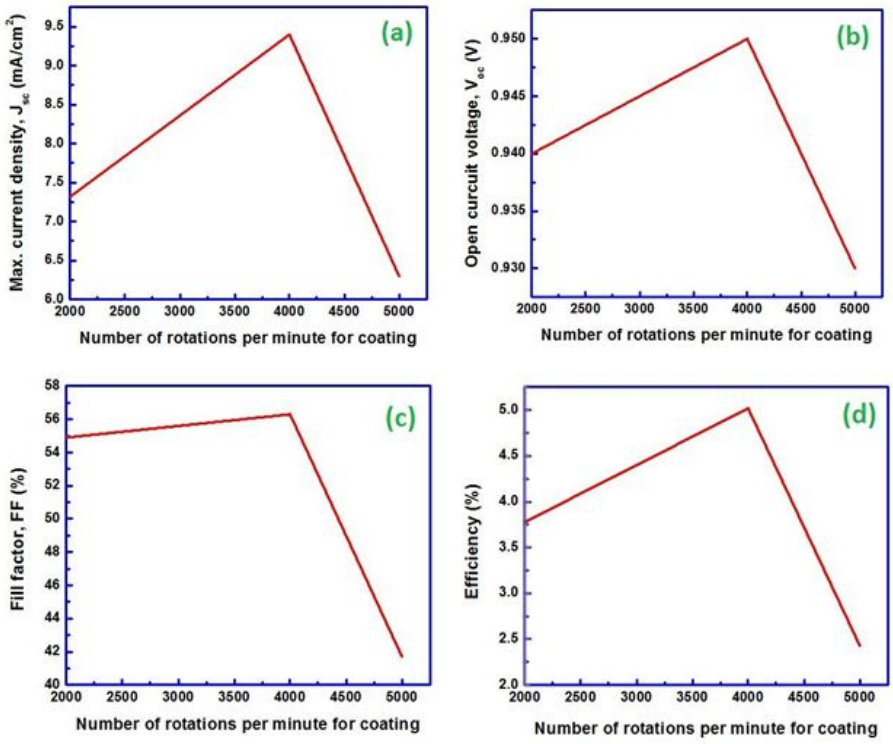

Figure 4.14: Plot of various parameters vs. number of rotations per minute used for coating of Zn_2SnO_4, (a) comparison plot for maximum obtained current density, J_{sc}, (b) comparison plot for maximum obtained open circuit voltage (V_{oc}), (c) comparison plot for maximum obtained fill factor value and (d) comparison plot for maximum obtained solar cell efficiency.

Curves in fig. 4.14 are plotted to show the dependence of parameters like current density (4.14 (a)), open circuit voltage (4.14 (b)), fill factor (4.14 (c)) and solar cell efficiency (4.14 (d)) on the number of rotations per minute used for making films of Zn_2SnO_4 through spin coating method. We can see the best performance for all the four cases have been obtained for the solar cell in which Zn_2SnO_4 is spin coated at 5,000 rotations per minute. Hence, material thickness is an important factor which determines the performance of a solar cell. Therefore an impressive photovoltaic efficiency of 5% was obtained with

Zn_2SnO_4 as electron transport layer in perovskite based solid state solar cells.

4.5 Conclusion

In conclusion we investigated the Zn_2SnO_4 as electron transport layer in sensitized solar cells with liquid as well as solid state hole conductors. In particular the thickness of Zn_2SnO_4 were optimized to obtain a maximum power conversion efficiency of 4.12% with N719 as sensitizer and I-/I3- as electrolyte. We also checked the quantum dot sensitized solar cells based on Zn_2SnO_4 as electron transport layer and CdS as sensitizer. The photovoltaic performance of CdS sensitized solar cells however was lower possibly because of poor light harvesting ability of CdS or increased recombination at the CdS-electrolyte interface. We further investigated the use of Zn_2SnO_4 as electron transport layer in organometal halide perovskite ($CH_3NH_3PbI_3$) sensitized solid state solsr cells. The spin coating speed in rpm was optimized to obtain optimum photovoltaic performance. An impressive photo-conversion efficiency of 5% was achieved in Zn_2SnO_4 based perovskite sensitized solid state solar cells which is among the highest value obtained for ZTO as electron transport layer.

Chapter 5

Future Scope

5.1 Mesoporous single crystal TiO_2

As we have seen in Chapter 3 that mesoporous single crystal (msc) $TiO_2$is an excellent material for Lithium ion battery application. This mscTiO_2 has highly accessible surface area therfore it can be also used in other applications such as super capacitors, gas sensors, photovoltaics etc. Further we can make composites of msc $TiO_2$with other functional materials like graphene, g-C_3N_4, Fe_3O_4etc. to tune its opto-electronic properties. We can also functionalize pores of this material with carbon or carbon nanotubes in order to enhance its electronic conductivity. Further, the method used for its synthesis can also be used for synthesis of single crystal of other materials like Cu_2O, Cd_2SnO_4 etc. which are also potential candidates in the field of optoelectronic devices.

5.2 Zinc Stannate (Zn_2SnO_4) nanostructures

We have seen that Zn_2SnO_4can be efficiently used in dye sensitized as well as solid state sensitized solar cells. However the efficiency of Zn_2SnO_4 based sensitized solar cells is lower as compared to the benchmark TiO_2. Therefore in order to improvise the efficiency further the origin of lower photovoltaic performance of Zn_2SnO_4 can be investigated using electrochemical impedance spectroscopy and transient opto-electronic measurements. We can also exploit this material in other applications like supercapacitor, water splitting, photodiode etc. We can make composites of Zn_2SnO_4 with other spinel (say Mn_3O_4) or anti spinel (say Fe_3O_4) materials to tune its electrical and magnetic properties. For example Zn_2SnO_4/Fe_3O_4composite can be used as a magnetically separable photocatalyst.

Bibliography

[1] Flack W. W., Soong D. S., Bell A. T., and Hess D. W., "A mathematical model for spin coating of polymer resists", J. Appl. Phys., 1984, 56, 1199.

[2] LeBeau J. M., Findlay S. D., Allen L. J., and Stemme S., "Standardless Atom Counting in Scanning Transmission Electron Microscopy", Nano Lett., 2011, 11 (10), pp 4504–4504.

[3] Ding Y., Wang Z. L., "Structure Analysis of Nanowires and Nanobelts by Transmission Electron Microscopy", J. Phys. Chem. B., 2004, 108, 12280.

[4] Murphy A. B., "Solar Energy Materials and Solar Cells", 2007, 91, 1326.

[5] Khan Z., Khannam M., Vinothkumar N., De M., Qureshi M., "Hierarchical 3D NiO– CdS heteroarchitecture for efficient visible light photocatalytic hydrogen generation", Journal of Materials Chemistry 2012, 22, 12090.

[6] Heston N., "IPCE Monochromator User Guide Newport Oriel", (800) 714-5393.

[7] Bruce P. G., Scrosati B. and Tarascon J.-M., "Nanomaterials for Rechargeable Lithium Batteries", Angew. Chem., Int. Ed., 2008, 47, 2930–2946.

[8] Froschl T., Hormann U., Kubiak P., Kucerova G., Pfanzelt M., Weiss C. K., Behm R. J., Husing N. and Mehrens M. W., "High surface area crystalline titanium dioxide: potential and limits in electrochemical energy storage and catalysis", Chem. Soc. Rev., 2012,41, 5313–5360.

[9] Rohlfing D. F., Wark M., Brezesinski T., Smarsly B. M. and Rathousky J., "Highly Organized Mesoporous TiO_2 Films with Controlled Crystallinity: A Li- Insertion Study", Adv. Funct. Mater.,2007, 17, 123–132.

[10] Winter M., Brodd R. J., "What are Batteries, Fuel Cells and Supercapacitors?", Chem. Rev., 2004, 104, 4245.

[11] Palacin M. R., "Recent advances in rechargeable battery materials: a chemist's perspective", Chem. Soc. Rev., 2009, 38, 2565.

[12] Scrosati B., Hassounab J. and Sun Y., "Lithium-ion batteries. A look into the future", Energy Environ. Sci., 2011, 4, 3287.

[13] Cheng F., Liang J., Tao Z., and Chen J., "Functional Materials for Rechargeable Batteries", Adv. Mater. 2011, 23, 1695.

[14] Bogush, G. H., Tracy, M. A. & Zukoski, C. Z. "Preparation of monodisperse silica particles: control of size and mass fraction", J.Non-Cryst. Solids104, 95–106(1988).

[15] Crossland E. J. W., Noel N., Sivaram V., Leijtens T., Webber Jack A. A. & Snaith H. J., "Mesoporous TiO_2single crystals delivering enhanced mobility and optoelectronic device performance", Nature 495, 215–219 (14 March 2013).

[16] Burschka J., Pellet N., Moon S. J., Baker R.H., Nazeeruddin M. K., & Gratzel M., "Sequential deposiotion as a route to high-performance perovskite sensitized solar cells", Nature 499,316–319.

[17] Patoux S.; Masquelier C., "Lithium insertion into titanium phosphates, silicates, and sulfates", Chem. Mater. 2002, 14 (12), 5057−5068.

[18] Kumar P. S., Aravindan V., Sundaramurthy J., Thavasi V., Mhaisalkar S. G., Ramakrishna S., and Madhavi S., "High performance lithium-ion cells using one dimensional electrospunTiO_2 nanofibers with spinel cathode", RSC Adv., 2012, 2(21), 7983–7987.

[19] Liu S., Long Y. Z., Zhang H. D., Sun B., Tang C. C., Li H. L., Kan G. W., and Wang C., "Synthesis of porous$LiMn_2O_4$ hollow nanofibers by electrospinning with extraordinarily lithium storage properties", Adv. Mater.Res., 2012, 562, 799–802.

[20] L. F. Shen, C. Z. Yuan, H. J. Luo, X. G. Zhang, K. Xu and F. Zhang, "In situ growth of $Li_4Ti_5O_{12}$ on multi walled carbon nanotubes: novel coaxial nanocables for high rate lithium ion batteries", J. Mater. Chem., 2011, 21, 761.39.

[21] P. G. Bruce, B. Scrosati and J.-M. Tarascon, "Nanomaterials for Rechargeable Lithium Batteries", Angew. Chem., Int. Ed., 2008, 47(16), 2930–2946.

[22] Baruah S. and Dutta J., Sci. Technol. Adv. Mater. 12 (2011) 013004.

[23] Kamat P. V., "Quantum Dot Solar Cells. The Next Big Thing in Photovoltaics", J. Phys. Chem. Lett. 2013, 4, 908−918.

[24] Tan B., Toman E., Li Y., and Wu Y., "Zinc Stannate (Zn_2SnO_4) Dye-Sensitized Solar Cells", J. AM. Chm. Soc., 2007,129, 4162-4163.

[25] Ito S., Chen P., Comte P., Nazeeruddin M. K., Liska P., Pechy P. & Gratzel M., "Fabrication of Screen-Printing Pastes From TiO_2 Powders for Dye-Sensitised Solar Cells", Prog. Photovolt: Res. Appl. 2007; 15:603–612.

[26] Zhang R., Luo Q., Chen H., Yu X., Kuang D., Su C. Y., "CdS/CdSe Quantum Dot Shell Decorated Vertical ZnO Nanowire Arrays by Spin-Coating-Based SILAR for Photoelectrochemical Cells and Quantum- Dot-Sensitized Solar Cells", ChemPhys, 2012, 13, 1435 – 1439.

[27] Dualeh A., Moehl T., Nazeeruddin M. K., and Gratzel M., "Temperature Dependence of Transport Properties of Spiro-MeOTAD as a Hole Transport Material in Solid-State Dye-Sensitized Solar Cells", ACS Nano, 2013,13,2292-2301.

[28] Burschka J., Pellet N., Moon S., Baker R.H., Gao P., Nazeeruddin M.K, & Grätzel M., "Sequential deposition as a route to high-performance perovskite-sensitized solar cells", Nature 499,316–319.